Chapter 3 Type-II CdSe@ZnTe and CdTe@CdSe Core/Shell Quantum Dots and their Properties

3.1. Introduction

Most type-II nanocomposites of II-IV elements reported thus far have been grown by molecular beam epitaxy.[1,2] Very recently, based on a colloidal template, an exquisite synthetic route to type-II CdSe@ZnTe and CdTe@CdSe (core/shell) QDs was achieved.[3] This soft-template approach is remarkable in that it offers both feasibility and versatility toward further chemical modification. The associated emission properties have been systematically analyzed for CdTe@CdSe. But the corresponding data on CdSe@ZnTe is obscure, possibly due to its weak interband emission at the NIR region.[3] Contrast to the thorough investigations of the electron/hole relaxation pathways on the type-I nanoparticles discussed in chapter 2,[4-12] to our knowledge, dynamics of the interfacial electron/hole separation for these type-II QDs has not been systematically studied. We herein present the spectroscopy and femtosecond upconversion approaches for type-II QDs, CdSe@ZnTe and CdTe@CdSe. The QDs were synthesized via an alternative synthetic route incorporating the greener and safer CdO (core), sulfur powder (shell) and zinc stearate (shell) as precursors instead of Cd(Me)$_2$ and (TMS)$_2$Se.[3]

3.2. Experimental Section

3.2.1. Chemicals

Tri-n-octylphosphine oxide (TOPO, 99 %), tri-n-butylphosphine (TBP, tech. grade 98 %) and hexadecylamine (HDA, 90 %) were purchased from Aldrich, SHOWA and TCI, respectively. CdO (99.99 %), CdCl$_2$ (99.99 %), selenium (Se)

powder 200 mesh (> 99.5 %), sulfur (S) powder (99.5 %) and Tellurium (Te) powder 200 mesh (99.8 %) were obtained from Strem, Adrich, ACROS, Alfa Aesar and Aldrich respectively. Zinc stearate was purchased from Riedel-deHaën.

3.2.2. Synthetic procedure

3.2.2.1 CdSe@ZnTe QDs

The preparation of the CdSe core from CdO was done according to previously reported by Peng and his co-workers[13] with a slight modification. Briefly, a Se injection solution containing 0.079 g of Se (1 mmol) was prepared in a gloved box by dissolving Se powder in 0.3 mL of tri-n-butylphosphine and then diluted it with 1.681 g di-n-octylamine. After that Se injection solution was brought out from the glovebox in a vial sealed with a rubber subseal. A mixture of CdO (0.0128 g, 0.10 mmol) and stearic acid (0.114 g, 0.40 mmol) was heated upto 140 °C in a three-neck flask under Ar flow. After CdO was completely dissolved, the mixture was cooled down to room temperature. Respectively, 1.94 g of the TOPO and HDA was added to the flask, and the mixture was heated to 320 °C. At this temperature, the Se injection solution was injected into the hot solution quickly. The reaction mixture was allowed to cool to 290 °C for the growth of the CdSe nanocrystals. Various sizes of CdSe QDs were obtained by the time-period required to terminate the reaction upon cooling. CdSe QDs were then precipitated out from the growth solution by adding methanol.

For a typical protocol to obtain the CdSe@ZnTe core/shell nanoparticles, the precipitated CdSe QDs (0.020 g) were dispersed in TOPO (2.20 g) and HDA (1.26 g) then heated to 190 °C. On the other hand, zinc stearate (0.316 g) was dissolved in of TBP 2.5 mL upon gentle heating (ca. 80 °C). After cooling to room temperature, the resulting 0.2 M solution was mixed with 2.5 mL of a 0.2 M solution of Te in TBP. Using a syringe pump, this mixture was injected within 1 h into the reaction flask

containing the core nanocrystals at 190-200 °C. After the addition was completed the crystals were annealed at 190 °C for an additional 1-1.5 h. Various sizes of core/shell nanoparticles were obtained by adjusting the concentrations of zinc stearate and Te in TBP as well as the corresponding injection period.

3.2.2.2 CdTe@CdSe QDs

The preparation of the CdTe core from CdO was done according to a method previously reported by Peng and coworkers[14] with a slight modification. Briefly, a Te injection solution containing 0.063 g of Te (0.5 mmol) was prepared in a glovebox by dissolving Te powder in 0.7 mL of TOP. The Te injection solution was then brought out of the glovebox in a vial sealed with a rubber subseal. A mixture of CdO (0.0128 g, 0.10 mmol) and stearic acid (0.114 g, 0.40 mmol) was heated in a three-neck flask to 140 °C under Ar flow. After the CdO was completely dissolved, the mixture was allowed to cool to room temperature. 1.94 g of the TOPO and HDA was then added to the flask, and the mixture was heated to 320 °C. At this temperature, the Se injection solution was quickly injected into the hot solution. The reaction mixture was then cooled to 250~270 °C to allow the growth of the CdTe nanocrystals. Various sizes of CdTe QDs were obtained in the time-period allowed before termination of the reaction upon cooling. CdTe QDs were then precipitated out from the growth solution via the addition of methanol. Further purification was performed by centrifugation and twice re-precipitation from methanol.

To prepare the shell CdSe, attempts were made using precursor CdO instead of Cd(Me)$_2$.[3] Unfortunately, we failed to obtain a good yield of CdTe@CdSe core/shell, possibly due to the sparse solubility of CdO in TBP or TOP even at 300°C. Similarly, due to the prohibition of obtaining (TMS)$_2$Se, the CdSe shell was synthesized via an alternative synthetic route incorporating CdCl$_2$ (shell) and Se powder (shell) as

precursors. In a typical protocol to obtain the CdTe@CdSe core/shell nanoparticles, the precipitated CdSe QDs (0.020 g) were dispersed in TOPO (2.20 g) and HDA (1.26 g) before being heated to 190 °C. In addition, $CdCl_2$ (0.092 g) was dissolved in 2.5 mL of TBP upon gentle heating (ca. 80 °C). After being cooled to room temperature, the resulting 0.2 M solution was mixed with 2.5 mL of a 0.2 M solution of Se in TBP. With a syringe pump, this mixture was injected within 1h into the reaction flask containing the core nanocrystals at 190–200 °C. After the addition was completed, the crystals were annealed at 190 °C for an additional 1–1.5 h. Core/shell nanoparticles of various sizes were obtained by adjusting the concentrations of $CdCl_2$ and Se in TBP as well as the corresponding injection periods. The prepared CdTe@CdSe QDs were further purified by centrifugation and twice re-precipitation from methanol.
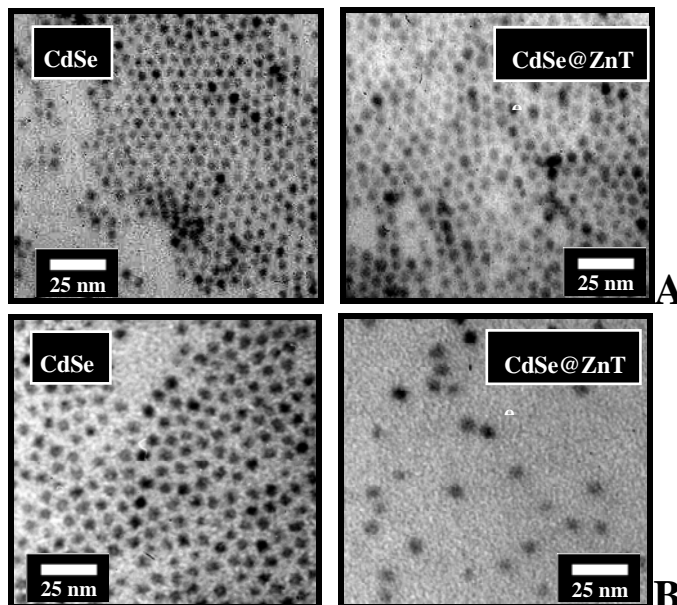
3.2.3. Measurement

The shapes of QDs were obtained with a Hitachi H-7100 transmission electron microscope (TEM). UV-Vis steady-state absorption and emission spectra were recorded by a Hitachi (U-3310) spectrophotometer and an Edinburgh (FS920) fluorimeter, respectively. The X-ray powder diffraction (XRD) pattern was characterized by a PANalytical X'Pert PRO (DY1894) spectrometer. The type-II NIR emission spectra were obtained by exciting the sample solution under a front-face excitation configuration using Ar ion laser (488 or 514 nm, Coherent Innova 90). The emission was then sent through an NIR-configured Fourier-transform interferometer (Bruker Equinox 55) and detected by a red sensitive photomutiplier (Hamamatsu model R5509-72) operated at −80 °C. Typically, the integration time for each measurement was about 15 minutes. Solvents such as toluene and tetrahydrofuran (THF) were of spectragrade quality (Merck Inc.) and used right after received.

Nanosecond lifetime studies were performed by an Edinburgh FL 900 photon-counting system with a hydrogen-filled/or a nitrogen lamp as the excitation source. The emission decays were analyzed by the sum of exponential functions, which allows partial removal of the instrument time broadening and consequently renders a temporal resolution of ~ 200 ps. The fluorescence dynamics in the pico-femtosecond region were measured using a femtosecond fluorescence upconversion system (FOG100, CDP Lasers & Scanning Systems). Briefly, the fundamental of a Kerr lens mode-locked titanium (Ti): sapphire laser (Tsunami, Spectra-Physics) pumped by an Argon laser (BeamLok 2060, Spectra-Physics) at 770–810 nm with an average power of 800 mW and a repetition rate of 82 MHz was used as the light source. About 500 mW of this output was frequency-doubled in a 0.5 mm BBO crystal. The frequency-doubled pulses were focused on the sample located in a rotating cell. The fluorescence was collected with an achromatic doublet. The unconverted pulses were sent along an optical delay line before being focused together with the fluorescence on a 0.5 mm BBO crystal. The polarization of the pump pulses was at the magic angle (54.7°) with respect to that of the gate pulses at 800 nm to eliminate the fluorescence anisotropy. The upconverted signal was sent into a spectrograph and its intensity was measured with a photomultiplier tube operated at the photon counting mode. The full width at half-maximum (fwhm) of the response function of the setup, measured by autocorrelation, was about 150 fs and 260 fs.

3.3. Results and Discussion

3.3.1 CdSe@ZnTe QDs

Figure 3.1 depicts TEM images of various sizes of CdSe@ZnTe type-II QDs and their initial core CdSe particles. The absorption and emission spectra of the CdSe cores and the corresponding CdSe@ZnTe type-II QDs are shown in Figure 3.2 and Figure 3.3,


Figure 3.1 TEM images of the samples with an average of **A)** 3.5 nm diameter CdSe QDs (left) and 4.3 nm CdSe@ZnTe QDs (right), **B)** 5.5 nm diameter CdSe QDs (left) and 6.3 nm CdSe@ZnTe QDs (right).

respectively, in which the core (core/shell) sizes, measured by TEM image, were calculated to be 3.5 (4.3), 4.1 (5.0) and 5.5 (6.3) nm in average.

Since CdSe@ZnTe QDs were prepared from the same batch of the CdSe precursor, the ZnTe thickness of three samples was derived to be 0.8, 0.9 and 0.8 nm, which, within experimental error, could be treated as a constant value. Thus, as shown in Figure 3.3, similar to that of core CdSe, the NIR emission
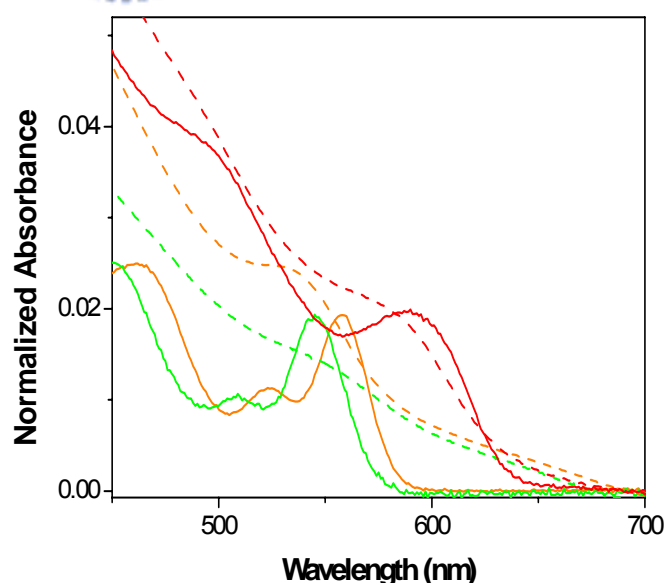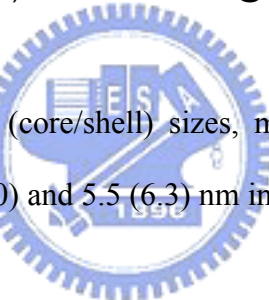
Figure 3.2 Absorption spectra of CdSe core (——) and CdSe@ZnTe core/shell (----) QDs in toluene by varying the core size from 3.5 nm (green), 4.1 nm (yellow) to 5.5 nm (orange). The thickness of the shell is ~0.8 ± 0.1 nm for all three cases.

band for CdSe@ZnTe QDs also revealed systematic red shift upon increasing the size of the CdSe core. The results, in combination with a rather narrow fwhm of ~1000–1300 cm^{-1}, rule out the possibility that the NIR emission bands result from a "deep trap" luminescence often observed in cores. In addition, a point worthy of note is that the synthetic route based on the CdO precursor resulted in a predominant CdSe core emission free of the deep-trap interference in this study. Thus, alternatively, it is more plausible to ascribe the NIR emission band originating from the radiative recombination of the electron-hole pair across the core/shell interface, i.e., the type II interband emission.[3] Theoretically, the energy gap of the interband emission correlates with the bandoffsets of the materials composing the core and the shell. If core/shell materials remain unchanged, the interband exciton emission should also be dependent on the size of the core and/or the thickness of the shell. This is clearly demonstrated in Figure 3.3.

Upon the increase in the size of CdSe cores from 3.5 to 5.5 nm, as indicated by the shift of the emission peak wavelength from 550 to 610 nm, the emission of CdSe@ZnTe, coated with a similar thickness (~0.8 nm)
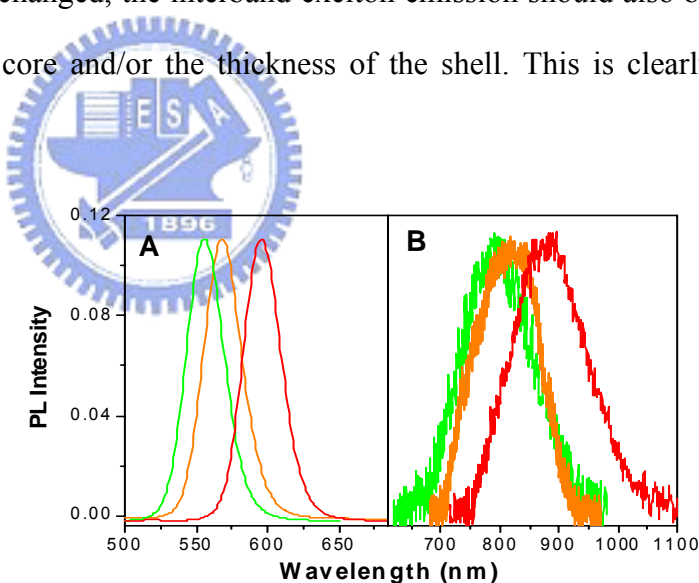
Figure 3.3 Emission spectra of CdSe core QDs and **B)** CdSe@ZnTe core/shell QDs in toluene by varying the core size from 3.5, 4.1 to 5.5 nm (from left to right).The thickness of the shell is ~0.8 ± 0.1 nm for all three cases. λ_{ex}: 488 nm.

of shell materials (ZnTe), shows a systematically bathochromic shift from 790 (core 3.5 nm@shell 0.8 nm) to 875 nm (core 5.5 nm@shell 0.8 nm). The results can be rationalized by lowering the CdSe conduction band at the edge, resulting in the decrease between the CdSe (higher band) and ZnTe (lower band) band gap.

Table 3.1 lists room-temperature luminescence decays for various sizes of CdSe and the corresponding CdSe@ZnTe QDs. The average population decay times for the core-only CdSe consistently decrease from 64 to 20 ns as the size of the core increases from 3.5 to 5.5 nm. Conversely, the average decay times of CdSe@ZnTe QDs, under the same shell thickness of ~0.8 nm, are about 50-55 ns with a lack of correlation with respect to the particle size. In contrast to the strong visible emission of the core ($\Phi_f >$ 0.5, see Table 3.1), the photoemission from CdSe@ZnTe QDs was observed at NIR region with relatively much weaker intensity. By comparing the emission intensity with that of *meso*-tetraphenylporphyrin ($\Phi_f \sim 0.11$) in toluene,[15] the quantum efficiency of the NIR interband emission was calculated to be on the order of 10^{-3} (see Table 3.1). The low emission yield, along with slow nonradiative processes (~50 ns), renders a radiative decay rate constant in the range of 10^4-10^5 s^{-1}, which is much

Table 3.1 Room temperature luminescence decays for various sizes of CdSe and corresponding CdSe@ZnTe QDs in toluene

CdSe Core				CdSe@ZnTe Core/Shell			
Size (nm)	PL (λ_{max})	$\tau_f^{\ b}$ (ns)	QY	Size^a (nm)	PL (λ_{max})	$\tau_f^{\ c}$ (ns)	QY ($\times 10^{-3}$)
3.5	555	63.7	0.51	4.3	790	55.7	4.77
4.1	570	42.5	0.55	5.0	815	52.4	4.09
5.5	610	19.9	0.56	6.3	875	53.8	3.81

^{a} core/shell size was synthesized from its corresponding core, and the average shell thickness was ~0.8 nm. ^{b} the average decay time at room temperature. ^{c} τ_f was measured at peak of the interband emission.

smaller than that of the core-only CdSe QDs by approximately three orders of magnitude (see Table 3.1). The extraordinarily long radiative lifetime can be rationalized by the slow, spatially separated electron-hole recombination of the excitons in type-II structures.
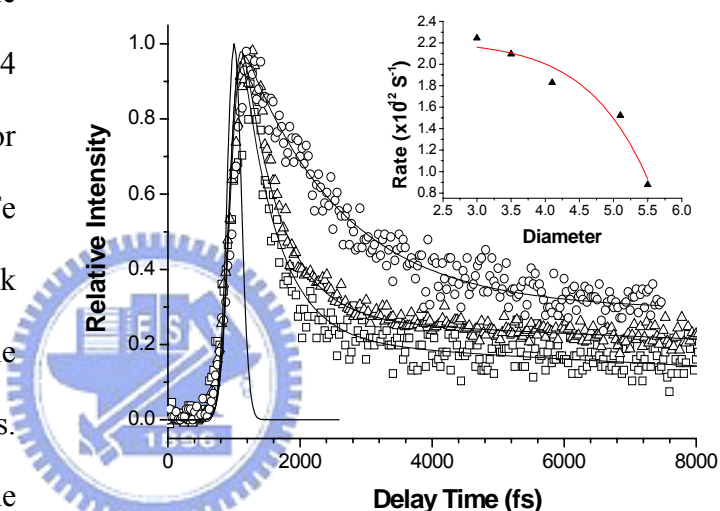
Femtosecond dynamics were performed to gain further insights into the dynamics of photoinduced electron-hole separation in the early stage. Based on the fluorescence upconversion technique, attempts to acquire the rise dynamics of the interband emission (> 700 nm) unfortunately failed mainly due to the exceedingly small radiative decay rate (vide supra). Alternatively, we have monitored the signal at the region of 550-630 nm supposed to be the precursor core emission, which, due to the dominant electron/hole pair spatially separated process, is negligibly small in the stead state intensity for the CdSe@ZnTe QDs. Figure 3.4 reveals the decay dynamics for various sizes of CdSe@ZnTe QDs monitored at the peak wavelength of the corresponding core CdSe QDs. It turned out that the experimental results could be qualitatively fitted well by two components: (1) a very fast but resolvable decay component, of

Figure 3.4 The fluorescence upconversion signal for CdSe@ZnTe QDs in toluene with a core diameter of (□) 3.5 nm (555 nm), (Δ) 4.1 nm and (○) 5.5 nm. (——) system response function. Emission is monitored at the peak wavelength of the corresponding core. Insert: The plot of electron-hole interfacial separation rate as a function of the core diameter. The thickness of shell (ZnTe) is ~ 0.8 nm for all QDs. λ_{ex}: 375 nm.

which the lifetime is within several hundred femtoseconds, and (2) a much slower component, of which the amplitude can be treated as a constant throughput the measured range of 10 ps. Component (2) was further resolved to be around 7-8 ns by the time-correlated single photon counting experiment.

Because the excitation wavelength was tuned at 375-400 nm in the fluorescence upconversion study, we realized that direct excitation of the ZnTe shell was also

possible.[16,17] Support of this viewpoint was rendered by both steady-state and nanosecond time-correlated single photon counting measurements shown in the insert of Figure 3.5, in which a weak emission with the peak wavelength of ~450 nm (τ_f ~ 7 ns) was resolved upon
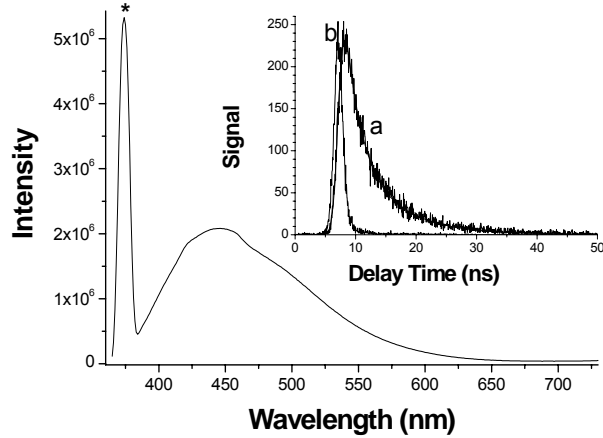
Figure 3.5 The steady-state emission of CdSe@ZnTe core/shell QDs (3.5/0.8 nm) excited at 375 nm. * denotes Rayleigh scattering. Insert: **a.** The decay dynamics monitored at 450 nm (τ_f ~ 7 ns, λ_{ex} = 375 nm), **b.** The system response function.

excitation at < 400 nm. In comparison, the 450 nm band was absent in the CdSe core QDs. Accordingly, the constant value shown in the upconversion experiment is most plausibly attributed to the directly excited ZnTe decay component. However, for the type-II CdSe@ZnTe QDs, the photoexcitation of the shell should result in a rapid electron transfer due to the same charge separated state as the core excitation. It is thus more likely to attribute the slow decay component to a small concentration of freestanding ZnTe particles, resulting from nucleation during the shell growth (vide infra).
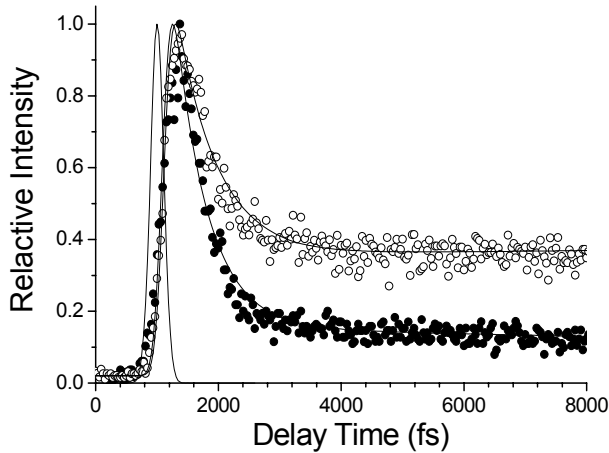
Figure 3.6 The same size of CdSe core (~5.1 nm) coated with (●) 0.8 nm and (○) 1.8 nm thickness of the ZnTe shell. (——) system response function. λ_{ex}: 375 nm.

As to the fast decay component, when the size of the CdSe core increased to 3.5, 4.1 and 5.5 nm, the rate of the decay component (1) systematically decreased to 477 ± 50 fs^{-1}, 547 ± 55 fs^{-1} and 1140 ± 70 fs^{-1}, respectively. Assuming that the

fast quenching of the core emission in CdSe@ZnTe is dominated by the rate of electron/hole spatial separation, the plot for the rate of interfacial hole-transfer versus the core diameter reveals a convex-curve-like correlation (see the insert of Figure 3.4). In contrast, a nearly shell-thickness independent rate of electron/hole spatial separation was observed. For example, by fixing the CdSe size at 5.1 nm, while the ZnTe thickness varied from 0.8 nm to 1.8 nm, the rates of fast decay component were measured to be 657 ± 50 fs^{-1} and 672 ± 60 fs^{-1}, respectively (see Figure 3.6), which, within experimental error, are identical. Note that in this case the NIR emission red shifts from 820 nm (core 5.1 nm@shell 0.8 nm) to 832 nm (core 5.1 nm@shell 1.8 nm, not shown here) possibly due to the increase of the ZnTe valence band at the edge. Furthermore, as shown in Figure 3.6, the intensity of the long decay component ($\tau_f \sim$ 7 ns) increases by $\sim$ two folds upon increasing the ZnTe thickness from 0.8 to 1.8 nm. Since the increase of shell thickness requires longer nucleation time for ZnTe, the freestanding ZnTe is expected to increase as well, providing a further support for the assignment of the 450 nm band to the ZnTe emission.

The above results, on the one hand, may be qualitatively rationalized in terms of a Coulombic interaction between the electrons and the holes that participate in the interband transition. If one assumes the quenching of the core emission in type-II QDs to be dominated by the hole tunneling process, in a one dimensional approach (along the radius z direction), the hole-transfer rate k_t can be expressed as

$$k_t \propto \exp\left[-\int\sqrt{\frac{2mV(z)}{\hbar}}dz\right] \qquad (1)$$

Where $V(z)$ denotes the Coulomb barrier for a hole confined in the local potential minima at the edge of CdSe. Theoretical approaches based on the variation method have shown that both height and width of $V(z)$ are dependent on the size of the core

(CdSe).[4-12,15] Electrons that are strongly confined in the CdSe layer create Coulomb wells at the center of the CdSe valence barriers. Thus, with larger sizes of CdSe QDs, the local potential minimum can confine the majority of photo-generated holes so that the hole-transfer into the ZnTe becomes more difficult. Unfortunately, the self-consistent approach for the potential energy surface of $V(z)$ cannot be solved exactly in Eq. (1), so that its application to fit the experimental results is infeasible. Nevertheless, this simple approach qualitatively predicts a core-radius dependent hole-tunneling rate. On the other hand, it is also possible that the finite rate of charge separation is due to the low electron-phonon coupling, causing there to small coupling between the initial and charge-separated states. Thus, a mechanism incorporating energy dissipation or coupling bottleneck[16,17] might be more plausible. Nevertheless, due to the lack of fundamental basis, the actual mechanism of relaxation dynamics remains unsolved, which should bring up a broad spectrum of interest in both experimental and theoretical approaches in the future.

3.3.2 CdTe@CdSe QDs

Figure 3.7 depicts TEM images of CdTe core and CdTe@CdSe core/shell type-II QDs. The corresponding composition was characterized by energy dispersive spectroscopy (EDX). As shown in Figure 3.8A, the appearance of the Se peak at 1.4 keV, in
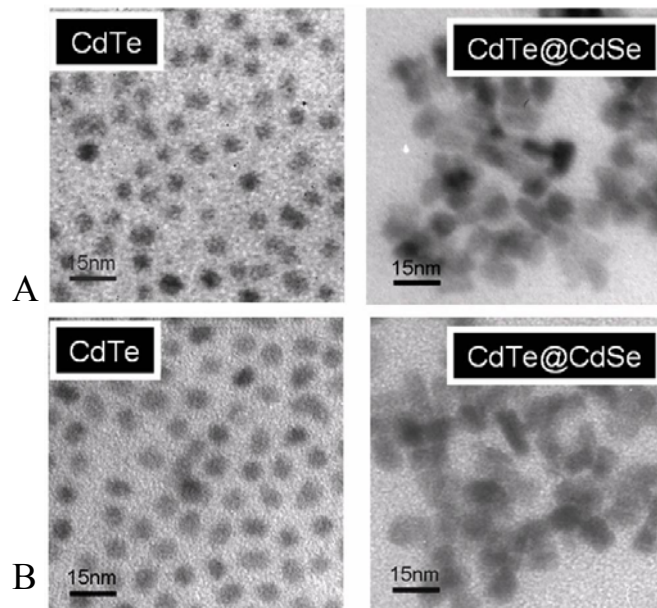
Figure 3.7 TEM images of the samples with an average of **A)** 6.0 nm diameter CdTe QDs (left) and 8.1 nm CdTe@CdSe QDs (right) **B)** 6.7 nm diameter CdTe QDs (left) and 8.9 nm CdTe@CdSe QDs (right)

combination with the increase of the ratio for Cd versus Te from 1.2:1 in CdTe to 6:1 in CdTe@CdSe, indicates the formation CdSe. As shown in Figure 2B, comparing the XRD pattern (not shown here) of the CdTe core, two sets of peaks at faces (100), (002), (101) and (110), (103), (112)
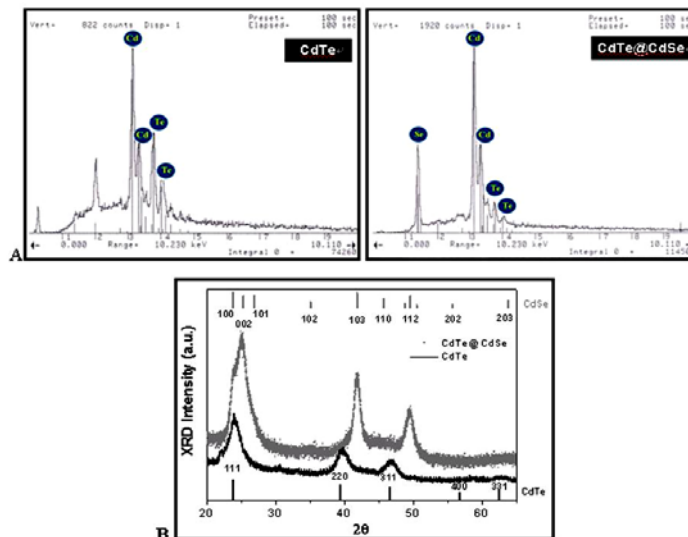

Figure 3.8 (upper) **A.** Energy dispersive spectroscopy (EDX) characterization of CdTe core (left) and CdTe@CdSe core/shell (right) nanocrystals prepared from CdCl$_2$ precursor described in the text. (lower) **B.** X-ray diffraction (XRD) data on CdTe cores (left) and CdTe@CdSe core/shell nanocrystals. (right)

shift to higher scattering angle upon coating CdSe shell, the results of which are consistent with that reported of the Kui Yu et al.[18] In addition, alloy, if it formed, should be supported by narrowing FWHM regarding the set of peaks at (100), (002) and (101). In contrast, a slight increase of FWHM was observed upon encapulating CdSe, supporting the formation of CdTe@CdSe core/shell structure.

To gain more detailed insights into the composition information we have further made much effort to perform XPS analyses. However, the Cd 3d$_{5/2}$ peak for CdTe and CdSe is nearly identical (404.8~405 eV[19,20]). This made us rather difficult to differentiate the core/shell structure form an alloy based on our current XPS system. Alternatively, the peak intensity ratio for elements of core versus shell as a function of the electron takeoff angle may serve as a valuable tool to extract geometrical information about nanoparticles.[21] Note that if QDs were composed of an alloy, the relative peak intensities for Se versus Te would be independent of the electron takeoff angle. Furthermore, empirically, the ratio of peak area for Te (3d$_{5/2}$) versus Se (3d) is

estimated to be 6.82 and 6.68 for X-ray sources at 90° and 54.7°, respectively.[22] Thus, upon normalizing the Se peak intensity, the peak intensity ratio for Te (90°): Te (54.7°) is deduced to be 1.02 for the case of a single layer. Figure 3.9 shows the XPS spectra of Se and Te peaks
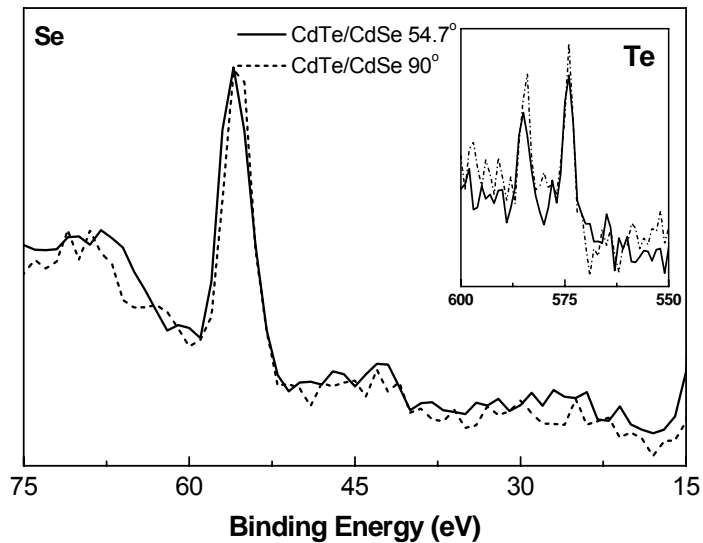

Figure 3.9 The normalized Se 3d XPS spectra of CdTe@CdSe aquired at different electron takeoff angle of 90° (----) and 54.7° (——). Insert: the peak intensity for Te 3d$_{5/2}$ at 90° (----) and 54.7° (——) upon normalization at the Se peak.

for the synthesized CdTe@CdSe QDs at incident angles of 90° and 54.7°, in which the Se peak intensity has been normalized. Accordingly, the intensity ratio for Te (90°):Te (54.7°) was caculated to be 1.26, which is greater than that of 1.02 deduced from a single layer, i.e. an alloy structure. Note that this derivation is based on the empirical data of bulk properties. Thus, the suitability for a similar approach toward nanoscale QDs may not be justified. For example, recently, Piyakis et al.[23] have reported the XPS analysis of spherical Cu nanoclusters. By using angle-resolved XPS, in combination with Monte Carlo simulation, they concluded that if the radius of the particle is larger than the attenuation length of the photoelectron, the angle dependence may lack good correlation. Nevertheless, the results of angle dependent XPS, in a qualitative manner, support the formation of CdTe@CdSe core/shell structure. More evidence of a type-II CdTe@CdSe core/shell structure is provided in the section of luminescence studies (vide infra).

The average sizes of both core only CdTe and CdTe@CdSe QDs can be

estimated directly from TEM. Unfortunately, the mismatch of the lattice constants between CdTe (6.48Å) and CdSe (6.05Å)[24] is only 7.1%, which is too small to resolve the core and shell individually via the difference in the lattice orientations from TEM. Since the CdTe@CdSe QDs were prepared from the same batch of the CdTe precursor, it is reasonable to assume the same core size in the CdTe@CdSe as in the core-only CdTe. Thus, as an indirect approach, the shell thickness can be estimated by the subtraction of the core size from that of the core/shell prepared.
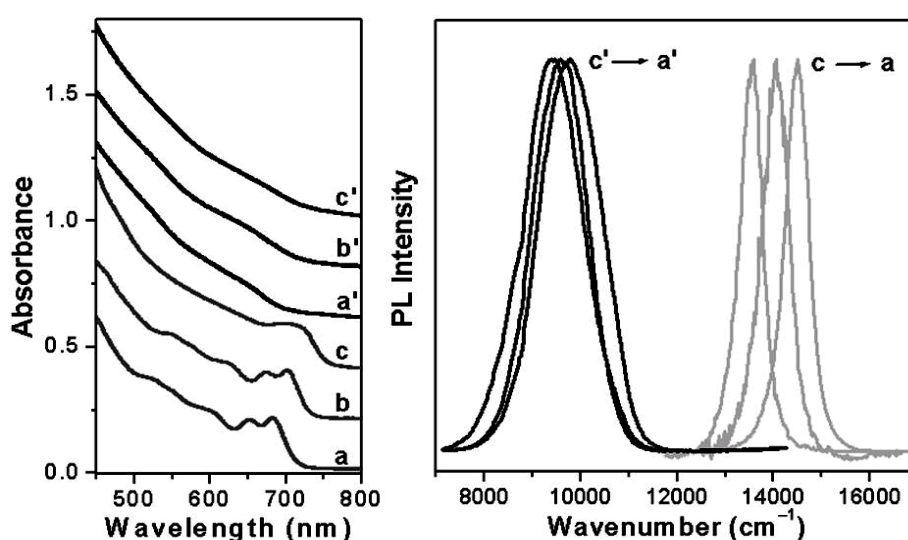
Figure 3.10 The absorption (left) and emission (right) spectra of CdTe core and CdTe@CdSe core/shell type-II QDs in toluene with different sizes, (a) 5.3 nm (core), (a') 6.3 nm (core/shell), (b) 6.1 nm (core), (b') 7.1 nm (core/shell), (c) 6.9 nm (core), (c') 7.8 nm (core/shell). The average thickness of the shell was estimated to be ~1.0 ± 0.2 nm. Note that the x-axis in the emission spectrum is in wavenumber (cm^{-1}) in order to show the real energy gap.

Figure 3.10 shows the absorption and emission spectra of the CdTe cores and the corresponding CdTe@CdSe QDs, in which the core (core/shell) sizes, measured by TEM size histograms, were calculated to be 5.3 (6.3), 6.1 (7.1) and 6.9 (7.8) nm (see Figure 3.7). Accordingly, the CdSe thicknesses of three samples were derived to be 1.0, 1.0 and 0.9 nm, which, within experimental uncertainty, could be treated as constant values. Considering that TEM generally provides insufficient contrast at the edges of nanoparticles, the measured sizes are subject to ~10 % uncertainty in average.

Similar to the CdTe core emission, the NIR interband emission band for CdTe@CdSe QDs also revealed size dependency. Theoretically, the energy gap of the interband emission should correlate with the band offsets of the materials composing the core and the shell. If shell thickness remains unchanged, the interband exciton emission should be dependent on the size of the core. This is clearly demonstrated in Figure 3.10. Upon the increase in the diameter of the CdTe cores from 5.3 to 6.9 nm, as indicated by the shift of the CdTe emission peak wavelength from 690 nm (14,493 cm^{-1}) to 737 nm (13,569 cm^{-1}), the emission of CdTe@CdSe, coated with a similar thickness (~1.0 nm) of shell materials (CdSe), shows a systematically bathochromic shift from 1025 nm (9,756 cm^{-1}, core 5.3 nm@shell 1.0 nm) to 1061 nm (9,425 cm^{-1}, core 6.9 nm@shell 0.9 nm). The results can be rationalized by raising the CdTe valence band, i.e. the decreasing of the oxidation potential,[25] upon increases in the CdTe size, at the edge, resulting in the decrease between the CdSe (higher band) and CdTe (lower band) band gap. Furthermore, the red shift in pure-core CdTe because of the change in size is 114 meV (from 690 to 737 nm), while the shift in the core/shell CdTe@CdSe QDs, assuming the same shell thickness, is 42 meV (from 1025 to 1061 nm), consisting with the model in that the recombination occurs from CdSe conduction band to the CdTe valence band (Type-II). By changing the size of CdTe core only, the shift in interband emission must be smaller than those for the emission within pure CdTe. Note that we also carefluy examined any possible emission band associated with alloy (such as CdTe$_x$Se$_{1-x}$), the peak wavelength of which is expected to be between that of CdTe core and CdTe@CdSe interband emission.[26] The lack of emission originating from alloy firmly supports the CdTe@CdSe core/shell formation. The results can be rationalized by raising the CdTe valence band, i.e. the decreasing of the oxidation potential, upon increases in the CdTe size, at the edge, resulting in the decrease between the CdSe (higher band) and CdTe (lower band) band gap (see

Figure 1.18).

Table 3.2. Room-temperature photophysical properties for various sizes of CdTe and corresponding CdTe@CdSe QDs in toluene

CdTe Core				CdTe@CdSe Core/Shell								
Size (nm)	PL (nm)	τ^a (ns)	QY (%)	Size^b (nm)	PL (nm)	$\tau_1{}^c$ (fs)	$\tau_2{}^c$ (fs)	$\tau_a{}^d$ (fs)	$\tau_b{}^{d,e}$ (ps)	$\tau_t{}^d$ (ps)	$\tau_b{}^f$ (ns)	QY (%)
6.0	687	21	15	8.1	968	150 (−0.49)	510 (0.51)	600 (−0.50)	105 (0.50)	1.8	51	3.1
6.7	705	36	12	8.9	1096	220 (−0.48)	690 (0.51)	720 (−0.50)	90 (0.50)	2.5	48	4.0
7.4	722	34	10	9.3	1211	280 (−0.49)	930 (0.50)	1050 (−0.50)	128 (0.50)	5.6	55	2.2

^{a} the average decay time at room temperature. ^{b} core/shell size was synthesized from its corresponding core, and the average shell thickness was ~2.1 nm. ^{c} the rise and decay components (see eq. (1) in text) measured at peak wavelength supposed for the core emission. ^{d} see eq. (2) in the text for the definition. Number in ( ) is the normalized preexponential value. ^{e} Due to the long-term photodecomposition the decay time obtained from fluorescence upconversion technique is much shorter than that obtained from the time-correlated single photon counting measurement in column ^{f}. Note that in fitting the interband emission), $1/\tau_D$ (see eq. (2)) is negligibly small in the time range of 30 ps and can thus be set as zero. In addition, the initial phase ϕ (see eq. (2)) is fixed to be 180º in all cases.

Table 3.2 lists room-temperature photophysical properties for CdTe of various sizes and the corresponding CdTe@CdSe QDs. The average population decay times for the core-only CdTe and CdTe@CdSe QDs are in the range of 20−40 ns and 45−60 ns, respectively. In contrast to the strong visible emission of the core ($\Phi_f \geq 0.1$, see Table 3.2), the NIR interband emission from CdTe@CdSe QDs is relatively weak. Through a comparison of the emission intensity with that of *meso*-tetraphenylporphyrin ($\Phi_f \sim 0.11$, $\lambda_{max} \sim 760$ nm) in toluene,[15] the quantum efficiency of the NIR interband emission was determined to be on the order of 10^{-2}–10^{-1} (see Table 3.2). For both CdTe and CdTe@CdSe QDs the emission quantum yields increased as the size of the core increased. This tendency might be rationalized, in part, by the formation of crystal defects, which then traps the exciton. Upon decreasing the core size, the surface-to-volume ratio becomes larger, and hence more amounts of defects may be developed. For the case of CdTe@CdSe QDs, the radiative decay rate was calculated to be in the range of 10^5–10^6 s^{-1}, which is smaller than that of the core-only CdTe QDs (10^7–10^8 s^{-1}) by approximately two orders of magnitude on average. The rather long radiative lifetime in CdTe@CdSe may be

rationalized by the slow, spatially separated electron-hole recombination of the excitons in type-II structures. Nevertheless, in comparison to the radiative decay rates of $10^4–10^5 \text{ s}^{-1}$ for the other type-II QDs such as CdSe@ZnTe,[27] the 10–100 fold increases of the radiative decay rate in CdTe@CdSe would allow us to probe the early relaxation dynamics of the interband emission via the femtosecond fluorescence upconversion approach, which are otherwise inaccessible for CdSe@ZnTe.[27]

Femtosecond dynamics were performed to gain further insights into the dynamics of the photoinduced charge separation in the early stage. In order to clearly elaborate the correlation, we have monitored the upconverted emission signal at both core and interband emission. The signal at the region of 650–720 nm, which is ascribed to the precursor core emission, is negligibly small in the steady state intensity for the CdTe@CdSe QDs due to the dominant charge separation process. Nevertheless, the upconverted fluorescence signal is relatively much higher than that of the interband emission due to its larger radiative decay rate (vide supra). Figure 3.10 reveals the decay dynamics for CdTe@CdSe QDs of various sizes monitored at the peak wavelength of the corresponding core CdTe QDs. It turned out that the temporal trace could be qualitatively well fitted by the convolution of pump-probe cross correlation with a full width at half maximum of ~260 fs in combination with an impulse response $I(t)$ expressed as
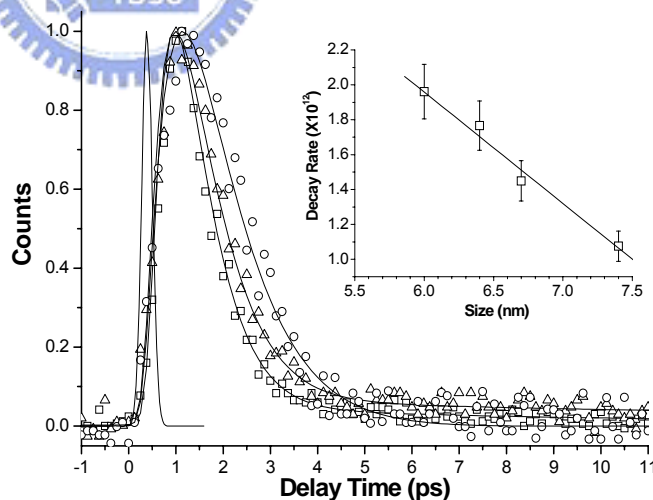
Figure 3.10 The fluorescence upconversion signal for CdTe@CdSe QDs in toluene with a core diameter of (□) 6.0 nm, (Δ) 6.7 nm and (○) 7.4 nm. Emission is monitored at the peak wavelength of the corresponding core, i.e., 687, 705 and 722 nm, respectively. (——) system response function. Insert: The plot of electron separation rate as a function of the core diameter. Note that an additional point of core (6.3 nm)@shell (2.1 nm) is added in the plot. The average thickness of shell (CdSe) is ~ 2.1 nm for all QDs. λ_{ex}: 390 nm.

$$I(t) = A + Be^{-t/\tau_1} + Ce^{-t/\tau_2} + De^{-t/\tau_3} \qquad \text{(eq. 1)}$$

Three single exponential components consist of (1) an ultrafast rise component, of which the rise time, within the experimental error, can be barely fitted to be ~160–280 fs; (2) a very fast decay component, of which the decay time, depending on the core size, was fitted to be several hundred femtoseconds to ~1 ps; and (3) a very long decay component (τ_3), with a very small, probably negligible amplitude that can be treated as a constant throughout the measured range of 15 ps. Component (3) was further resolved to be ~ 12–15 ns via the time-correlated single photon counting experiment. Table 3.2 lists the fitted parameters (τ_1 and τ_2) for those CdTe@CdSe QDs studied.

As for component (3), because the available excitation wavelength was tuned to 380–420 nm in the fluorescence upconversion study, it is possible that direct excitation of the CdSe shell was also possible.[4-12,15] Support of this viewpoint was given by both steady-state and nanosecond time-correlated single photon counting measurements, in which a weak emission with the peak wavelength of ~550 nm (τ_f ~ 13 ns, not shown here) was resolved upon excitation at < 400 nm. In comparison, the 550 nm band was absent in the CdTe core-only QDs. However, for type-II CdTe@CdSe QDs, photoexcitation of the shell CdSe should result in a very rapid electron transfer due to the same charge separated state as the core excitation. It is thus more plausible to attribute the very weak intensity, long decay component to a trace concentration of freestanding CdSe particles generated from the nucleation during the shell growth. Nevertheless, due to the small amplitude and long population decay, this component is simply neglected for the following discussion.

As to the fast decay component (2), when the size of the CdTe core increased to 6.0, 6.7 and 7.4 nm, the lifetime of the decay component (2) systematically increased to 510 ± 50 fs^{-1}, 690.2 ± 55 fs^{-1} and 930 ± 50 fs^{-1}, respectively. Assuming that the fast quenching of the core emission in CdTe@CdSe is dominated by the rate of photoinduced electron transfer to the shell, the plot for the rate of interfacial electron transfer versus the core diameter reveals a straight-line-like correlation (see the insert of Figure 3.10). The result seems to be in contrast to a similar plot with a convex-curve-like relationship for the CdSe@ZnTe type-II QDs. However, it should be noted that the plot for CdSe@ZnTe QDs is based on a large variation (~1.8 folds) of core size, ranging from 3.0 to 5.5 nm, while, due to the use of CdO precursor, the largest difference in the core size could be prepared is 1.4 nm (6.0–7.4 nm, ~1.25 folds) for the CdTe@CdSe QDs. Thus, unless a wider range of CdTe core sizes can be obtained, a fair comparison of charge separation rates between CdTe@CdSe and CdSe@ZnTe QDs is not meaningful. Note that syntheses of a smaller core size CdTe may be achieved via using more reactive $Cd(CH_3)_2$ as a precursor.[3] In contrast, a nearly shell-thickness independent rate of electron transport was observed. For example, with the CdTe size fixed at 6.7 nm, while the CdSe thickness varied from 1.2 nm to 2.2 nm, the rates of fast decay component were measured to be 490 ± 50 fs^{-1} and 510 ± 50 fs^{-1}, respectively. In this approach, the NIR emission red shifts from 1088 nm (core 6.7 nm@shell 1.2 nm) to 1100 nm (core 6.7 nm@shell 2.2 nm), possibly due to the decrease of the CdSe conduction band at the interfacial edge. Finally, although the time scale of the rise component (1) is within the borders of the detection response limit, it can still be barely resolved and appears to increase as the core size increases from 6.0 nm (~150 ± 60 fs) to 7.4 nm (~280 ± 70 fs). Since the excitation wavelengths of 380–410 nm are well above the lowest-lying conduction band of the CdTe core, we here tentatively propose that the finite rise component may

originate from a fast internal conversion, followed by the relaxation to the lowest conduction band. However, due to its nearly detection-response-limited time scale, we believe that any quantitative attempts to ascertain the corresponding mechanism will be based on too much speculation and hence may not be reliable.

3.4. Conclusions

In conclusion, we have prepared CdSe@ZnTe and CdTe@CdSe QDs from the greener CdO and $CdCl_2$ precursors for core and shell, respectively. The spectroscopy and dynamics of these type-II QDs interband emissions are studied. The hole transfer rate of CdSe@ZnTe as a function of the core/shell size has been systematically investigated. The results indicate that the rate of hole transfer decreases with increase in the size of the cores, and is independent of shell-thickness in the CdSe@ZnTe QDs. This degree of control can be especially crucial in applications where rapid carrier separation followed by charge transfer into a matrix or electrode is important, as in photovoltaic devices. Furthermore, based on the femtosecond upconversion technique, we report on the first observation of early relaxation dynamics on the CdTe/CdSe type-II QDs interband emission. The results indicate that the electron separation rate decreases as the size of the cores increases. Due to the lack of observing coherent optical phonon modes for both CdTe core (in CdTe/CdSe) emission and CdTe/CdSe interband emission, it is thus possible that the finite rate of charge separation is due to the low electron-phonon coupling, causing small coupling between the initial and charge-separated states. We believed that the results shown here, especially the degree of control on the rate of electron transfer, can be crucial in applications where rapid

carrier separation followed by charge transfer into a matrix or electrode is important, as in photovoltaic devices.

3.5.   References

1. Hatami, F.; Grundmann, M.; Ledentsov, N. N.; Heinrichsdorff, F.; Heitz, R.; Böhrer, J.; Bimberg, D.; Ruvimov, S. S.; Werner, P.; Ustinov, V. M.; Kop'ev, P. S.; Alferov, Z. I. *Phys. Rev. B* **1998**, *57*, 4635.

2. Youn, H. C.; Baral, S.; Fendler, J. H. *J. Phys. Chem.* **1998**, *92*, 6320.

3. Kim, S.; Fisher, B.; Eisler, H. J.; Bawendi, M. G. *J. Am. Chem. Soc.* **2003**, *125*, 11466.

4. Chikan, V.; Kelley, D. F. *Nano Lett.* **2002**, *2*, 141.

5. Chikan, V.; Kelley, D. F. *Nano Lett.* **2002**, *2*, 1015.

6. Tu, H.; Chikan, V.; Kelley, D. F. *J. Phys. Chem. B* **2003**, *107*, 10389.

7. Woggon, U.; Geissen, H.; Gindele, F.; Wind, O.; Fluegel, B.; Peyghambarian, N. *Phys. Rev. B* **1996**, *54*, 17681.

8. Klimov, V. I.; McBranch, D. W. *Phys. Rev. Lett.* **1998**, *80*, 4028.

9. Guyot-Sionnest, P.; Shim, M.; Matranga, C.; Hines, M. *Phys. Rev. B* **1999**, *60*, R2181.

10. Klimov, V. I.; Schwarz, C. J.; McBranch, D. W.; Leatherdale, C. A.; Bawendi, M. G. *Phys. Rev. B* **1999**, *60*, R2177.

11. Klimov, V. I.; Milhailosky, A. A.; McBranch, D. W.; Leatherdale, C. A.; Bawendi, M. G. *Phys. Rev. B* **2000**, *61*, R13349.

12. Burda, C.; Link, S.; Mohamed, M.; El-Sayed, M. A. *J. Phys. Chem. B* **2001**, *105*, 12286.

13. Qu, L.; Peng, Z. A.; Peng, X. *Nano Lett.* **2001**, *1*, 333.

14. Peng, Z. A.; Peng, X. *J. Am. Chem. Soc.* **2001**, *123*, 183.

15. Seybold, P. G.; Gouterman, M. *J. Mol. Spectrosc.* **1969**, *31*, 1.

16. Lee, E. H.; Stoltz, S.; Chang, H. C.; Na, M. H.; Luo, H.; Petrou, A. *Solid State Commun.* **1998**, *107*, 177.

17. Haetty, J.; Lee, E. H.; Luo, H.; Petrou, A.; Warnock, J. *Solid State Commun.* **1998**, *108*, 205.

18. Yu, K.; Zaman, B.; Romanova, S.; Wang, D.; Ripmeester, J.A., *Small* **2005**, *1*, 332.

19. Briggs, D.; Seah, M.P., *John WILLEY & SONS.*, **1993**, *Vol. 1,* second edition.

20. Wagner, C.D.; Moulder, J.F., Davis, L.E.; Riggs, W.M., *Physical Electronics Division*, Perking-Elmer Corporation, (end of book).

21. Tunc, I.; Suzer, S.; Correa-Duarte, M.A.; Liz-Marzan, L.M., *J. Phys. Chem. B* **2005**, *109*, 7597.

22. Wagner, C.D.; Davis, L.E.; Zeller, M.V.; Taylor, J.A.; Raymond, R.H.; Gale, L.H., *Surf. Interface Anal.* **1981**, *3*, 211.

23. Piyakis, K.N.; Yang, D.-Q.; Sacher, E., *Surf. Sci.* **2003**, *536*, 139.

24. Sze, S.M., *Physics of Semiconductor Device*, New York, Wiley Interscience Publication, **1981**, p. 848-849.

25. Kucur, E.; Riegler, J.; Urban, G.A.; Nann, T., *J. Chem. Phys.* **2003**, *119*, 2333.

26. Bailey, R.E.; Nie, S., *J. Am. Chem. Soc.* **2003**, *125*, 7100.

27. Chen, C.Y.; Cheng, C.T.; Yu, J.K.; Pu, S.C.; Cheng, Y.M.; Chou, P.T.; Chou, Y.H.; Chiu, H.T., *J. Phys. Chem. B* **2004**, *108*, 10687.

Chapter 4   Syntheses and Photophysical Properties of Type-II CdSe@ZnTe@ZnS and CdSe@CdTe@ZnTe Core/Shell/Shell Quantum Dots

4.1. Introduction

One intriguing potential of the type II QDs is to greatly extend the lifespan of the charge separation, so that either electron or hole floating on the outmost shell region can be further exploited in variety of applications. Among which the use of type II QDs as a catalyst in the redox reaction is of particular importance. In view of this goal we have carried out the following design strategy toward a core/shell/shell type II QDs. Here, we propose two types of structures A and B for investization. For the structure A shown in Scheme 4.1A, the valence band of ZnS is below that of ZnTe, while both vanelnce and conduction bands in ZnTe are well above that in CdTe, forming a cascade type of band edges in a sequence of CdSe < CdTe < ZnTe.As shown in Scheme 4.1B, the conduction band of the structure B in ZnTe is well above

that in CdSe. Upon excitation, the electrons and the holes in the structure A are strictly confined in CdSe and ZnTe, respectively, encapsulated by ZnS. Thus, floating of the hole-carrier on the surface of ZnS can be significantly reduced,
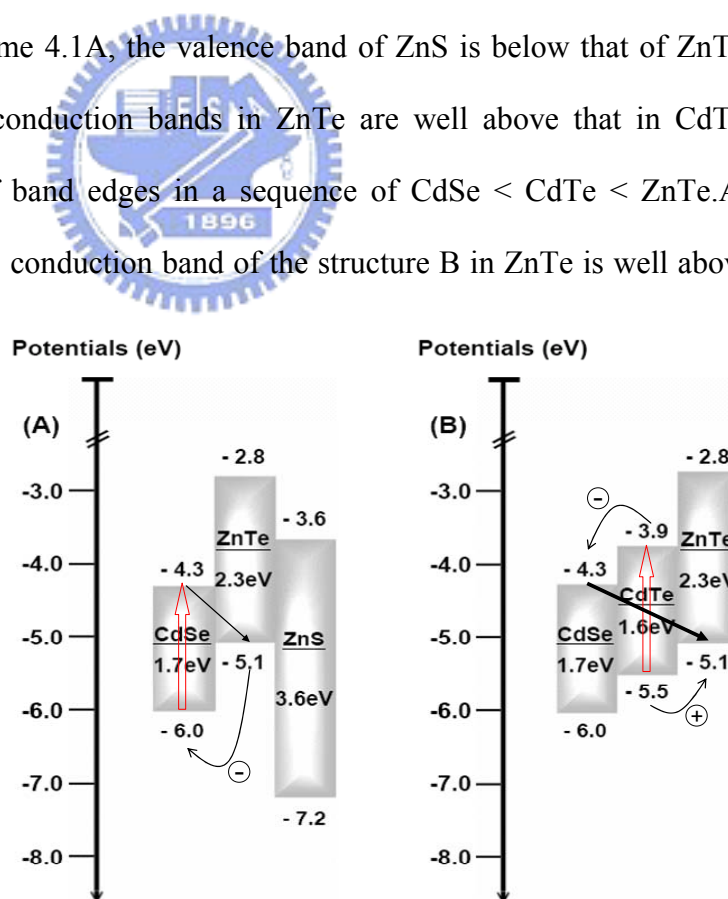
Scheme 4.1 Plot illustrating the aligment of CdSe, CdTe, ZnTe and ZnS band offsets. Note that the energy level of band edges is taken from bulk properties of the corresponding materials. In addition, subtle changes of the band gap and hence the relative energies in the interfacial regions are neglected in this diagram.

resulting in the enhancement of CdSe → ZnTe interband emission intensity. For the structure B, upon excitation, as shown in Scheme 4.1B, the electrons and the holes are still confined in CdSe and ZnTe, respectively. Thus, the lowest lying elecron/hole combination should originate from CdSe (electron) and ZnTe (hole). In this case the rate of recombination is expected to be rather slow because charge separation is enhanced via an intermediate CdSe layer. Thus, in additon to their synthetic challenges and future application perspectives, the associated photophysical peoperties of core/shell/shell type II QDs are important. Detailed results and discussion are elaborated as follows.

4.2. Experimental Section

4.2.1. Chemicals

Tri-*n*-octylphosphine oxide (TOPO, 99 %), tri-*n*-butylphosphine (TBP, technical grade 98 %, SHOWA), di-*n*octylamine (DOA, 98%, ACROS), hexadecylamine (HDA, 90 %, TCI), CdO (99.99 %, Strem), selenium (Se) powder 200 mesh (99.5 %, Aldrich)**,** sulfur (S) powder (99.5%, Aldrich) , CdCl$_2$ (99.99%, Aldrich), tellurium (Te) powder (99.8 %, 200 mesh, Aldrich) and zinc stearate (Riedel-deHaën) were used immediately after receipt.

4.2.2. Synthetic procedure

4.2.2.1 CdSe@ZnTe@ZnS QDs

The CdSe@ZnTe core/shell nanoparticles were prepared according to our previous report.[1] To obtain the CdSe@ZnTe@ZnS core/shell/shell nanoparticles, the precipitated CdSe@ZnTe QDs (0.020 g) were dispersed in TOPO (2.20 g) and HDA (1.26 g) before being heated to 190 ℃. In addition, Zn stearate (0.316 g) was

dissolved in 2.5 mL of TBP upon gentle heating (ca. 80 ℃). After being cooled to room temperature, the resulting 0.2 M solution was mixed with 2.5 mL of a 0.2 M solution of S in TBP. With a syringe pump, this mixture was injected within 1h into the reaction flask containing the core/shell nanocrystals at 190-200 ℃. After the addition was completed, the crystals were annealed at 190 ℃ for an additional 1-1.5 h. CdSe@ZnTe@ZnS QDs of various ZnS thickness could be obtained by adjusting the concentrations of Zn stearate and S in TBP as well as the corresponding injection periods. The resulting CdSe@ZnTe@ZnS QDs were further purified by centrifugation and twice re-precipitation from methanol. The water-soluble CdSe@ZnTe@ZnS nanoparticles were prepared using a stepwise procedure reported by Mattoussi et al.[2] with a slight modification. Briefly, TBP/TOPO-capped CdSe@ZnTe@ZnS core/shell/shell particles were subsequently exchanged with 20 mg DHLA (freshly prepared from distilled thioctic acid by sodium borohydride reduction)[3] placed in a reaction vessel. While 15 mL of methanol was added, the pH was adjusted to > 10 with tetramethylammonium hydroxide pentahydrate. Under dark conditions, 10 mg of CdSe@ZnTe@ZnS nanocrystals were dissolved in the mixture, and the vessel was placed under regular airflow. The mixture was heated under reflux at 65 ℃ overnight, and then the reaction was terminated and the mixture was cooled to room temperature. The DHLA-capped nanocrystals were then precipitated with diethyl ether. For further purification, methanol was added to dissolve the precipitate, followed by the addition of diethyl ether to reprecipitate the nanocrystals.

4.2.2.2 CdSe@CdTe@ZnTe QDs

The preparation of the CdSe core from CdO was done according to a method previously reported by Peng and coworkers[4] with a slight modification. Briefly, a Se injection solution containing 0.079 g of Se (1 mmol) was prepared in a glovebox by

dissolving Se powder in 0.3 mL of TBP. The Se injection solution was then brought out of the glovebox in a vial sealed with a rubber subseal. A mixture of CdO (0.0128 g, 0.10 mmol) and stearic acid (0.114 g, 0.40 mmol) was heated in a three-neck flask to 140 °C under Ar flow. After the CdO was completely dissolved, the mixture was allowed to cool to room temperature. 1.94 g of the TOPO and HDA was then added to the flask, and the mixture was heated to 320 °C. At this temperature, the Se injection solution was quickly injected into the hot solution. The reaction mixture was then cooled to 250~270 °C to allow the growth of the CdSe nanocrystals. Various sizes of CdSe QDs were obtained in the time-period allowed before termination of the reaction upon cooling. CdSe QDs were then precipitated out from the growth solution via the addition of methanol. Further purification was performed by centrifugation and twice re-precipitation from methanol.

To prepare the shell CdTe, we used $CdCl_2$ (shell) and Te powder (shell) as precursors. In a typical protocol to obtain the CdSe@CdTe core/shell nanoparticles, the precipitated CdSe QDs (0.020 g) were dispersed in TOPO (2.20 g) and HDA (1.26 g) before being heated to 190 °C. In addition, $CdCl_2$ (0.117 g) was dissolved in 3 mL of TBP upon gentle heating (ca. 80 °C). After being cooled to room temperature, the resulting 0.2 M solution was mixed with 3 mL of a 0.2 M solution of Te in TBP. With a syringe pump, this mixture was injected within 1.5 h into the reaction flask containing the core nanocrystals at 190–200 °C. After the addition was completed, the crystals were annealed at 190 °C for an additional 1–1.5 h. Core/shell nanoparticles of various sizes were obtained by adjusting the concentrations of $CdCl_2$ and Te in TBP as well as the corresponding injection periods. The prepared CdSe@CdTe QDs were further purified by centrifugation and twice re-precipitation from methanol.

The CdSe@CdTe@ZnTe (core/shell/shell) QDs was prepared from passivating the CdSe@CdTe by ZnTe. In this approach, Zn stearate and Te powder (shell) were used as the precursors. In a typical protocol to obtain the CdSe@CdTe@ZnTe core/shell/shell nanoparticles, the precipitated CdSe/CdTe QDs were dispersed in TOPO and HDA prior to the reflux. In addition, Zn sterate was dissolved in 3 mL of TBP upon gentle heating (ca. 80 °C). After being cooled to room temperature, the resulting 0.2 M solution was mixed with 3 mL of a 0.2 M solution of Te in TBP. With a syringe pump, this mixture was injected within 1.5 h into the reaction flask containing the core nanocrystals at 190–200 °C. After the addition was completed, the crystals were annealed at 190 °C for an additional 1–1.5 h. Various of ZnTe shell thickness could be obtained by adjusting the concentrations of Zn stearate and Te in TBP as well as the corresponding injection periods. The resulting CdSe@CdTe@ZnTe QDs were further purified by the same way with CdSe@CdTe core/shell.
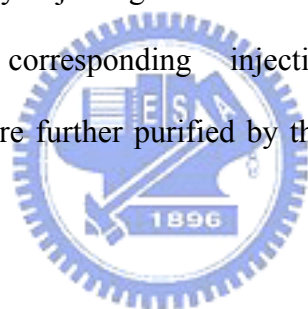
4.2.3 Measurements

The sizes of QDs were determined with a Hitachi H-7100 transmission electron microscope (TEM). Further characterization of QDs was made with powder X-ray diffraction (XRD, model PANalytical X' Pert PRO) and X-ray photoelectron spectroscopy (XPS, model VG Scientific ESCALAB 250). UV-Vis steady-state absorption and emission spectra were recorded with a Hitachi (U-3310) spectrophotometer and an Edinburgh (FS920) fluorimeter, respectively. The NIR emission spectra were obtained by exciting the sample solution under a front-face excitation configuration using an Ar ion laser (488 or 514 nm, Coherent Innova 90). The emission was then sent through an NIR-configured Fourier-transform

interferometer (Bruker Equinox 55) and detected with a NIR sensitive photomutiplier (Hamamatsu model R5509-72, operated at -80 $^{\circ}$C) coupled with a Lock-in Amplifier (Stanford Research System SR830) and a monochromator (Acton, SpectraPro-275) in that the grating was blazed at 1200 nm. The NIR fluorescence was collected at a direction perpendicular to the pump beam. To minimize the re-absorption effect, the excitation beam was focused as closely as possible to the front wall of the quartz cell. For the NIR lifetime measurement, the sample was excited by a 532 nm pulse (2nd harmonic of Nd:YAG, 6 ns). The emission trace was detected by a photomultiplier tube (Hamamatzu R5509-72) operated at -80 $^{\circ}$C and recorded by a sampling oscilloscope (Tektronix, TDS 3012). An average of 100 shots was taken in the lifetime measurement, unless specified elsewhere. IR125 with an emission yield of $\Phi \sim 0.11$ ($\lambda_{max} \sim 910$ nm) in DMSO (dimethylsulfoxide) served as a standard to calculate the emission quantum yield.[5] For the measurement of the two-photon absorption cross section, a mode-locked femtosecond Ti:Sapphire laser (Spectra-physics, 100 fs, 80 MHz) pumped Opal (Spectra-physics, 130 fs, 80 MHz) was used as an excitation source. Dye 5,10,15,20-tetraphenylporphine (H_2TPP, Aldrich) was used as a standard, of which the two-photon absorption cross section (σ) was reported to be s 3.5 GM (1 GM = 10^{-50} cm^4 s photon^{-1}) upon 1200-nm excitation in toluene.[6]

4.3. Results and Discussion

4.3.1 CdSe@ZnTe@ZnS QDs

Figure 4.1 depicts TEM images and size histograms of CdSe@ZnTe (core/shell) and CdSe@ZnTe@ZnS (core/shell/shell) in which the core/shell (CdSe@ZnTe) QDs are from the same batch. The size histograms of CdSe@ZnTe and CdSe@ZnTe@ZnS QDs were established via counting each individual size over 500 particles. Since the

CdSe@ZnTe@ZnS QDs were prepared from the same batch of CdSe@ZnTe, it is reasonable to assume the same core/shell size. As an indirect approach, the thickness of ZnS can be estimated by the subtraction of CdSe@ZnTe size from that of the CdSe@ZnTe@ZnS prepared. For QDs shown in Figure 4.1, the diameter of CdSe@ZnTe and CdSe@ZnTe@ZnS was measured to be in an average of 5.0 and 5.8 nm, respectively. Accordingly, the thickness of ZnS was estimated to be 0.4 nm. Considering that TEM generally provides insufficient contrast at the edges of nanoparticles, the calculated ZnS thickness could be subject to ~10-15 % uncertainty.
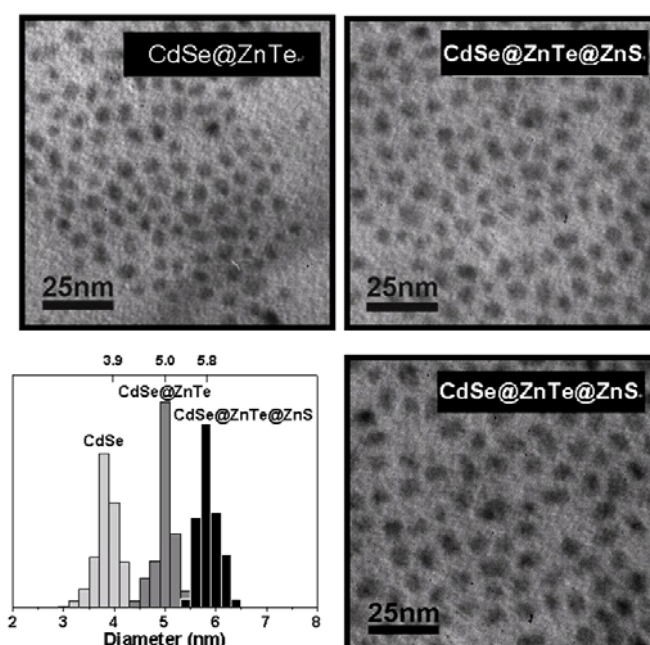

Figure 4.1 TEM images of the samples with an average of 5.0 nm CdSe@ZnTe QDs (upper-left) and 5.8 nm CdSe@ZnTe@ZnS QDs (upper-right) in diameter. (lower-left) Size histograms for the series of samples. The histograms were made via counting over 500 particles in each sample. (lower-right) CdSe@ZnTe@ZnS QDs of 6.6 nm (0.8 nm thickness in ZnS)

The corresponding composition of CdSe@ZnTe@ZnS was characterized by energy dispersive spectroscopy (EDX). As shown in Figure 4.2A, the appearance of the S peak at 2.33 keV, in combination with the increase of the ratio for Zn versus Te from CdSe@ZnTe to CdSe@ZnTe@ZnS, may indirectly support the formation of ZnS shell, although the possibility of alloy formation cannot be ruled out.

Furthermore, as shown in Figure 4.2B, comparing the XRD pattern of the CdSe@ZnTe core/shell, two sets of peaks at faces (100), (002), (101) and (110), (103), (112) in CdSe@ZnTe@ZnS QDs revealed the same spectral features, with slightly shift to lower scattering angle for (110), (103), (112) peaks. Owing to a similar XRD pattern for these two sets of peaks, the formation of an alloy upon encapsulating ZnS is not likely. Nevertheless, similar to the results of EDX, the X-ray data could not definitely conclude a core/shell/shell structure.

In an attempt to extract more composition information we have further made efforts to perform XPS analyses. However, as depicted in the supplementary information (SI), our results revealed negliglbly small differences in XPS peaks between CdSe@ZnTe and CdSe@ZnTe@ZnS systems for those Cd, Zn, Se and Te elements. The results may not be surprising. For the case of Cd $3d_{5/2}$ in CdSe and CdTe, photoelectron peaks were expected to locate at 404.8 eV[7] (or 405.0 eV[8]) and 405.0 eV[7] (or 404.8 eV[8]), respectively. Our results of ~405.4 eV, witihin experimental uncertainty, cannot be definitely distinguished. Alternatively, if one focuses on the Te $3d_{5/2}$ state, the resulting Te peak was located at 572.8 eV for both CdSe@ZnTe and CdSe@ZnTe@ZnS systems (see SI). In comparison, the corresponding peak for ZnTe is expected to be at 572.9 eV,[9] which is similar to that of CdTe of 572.7 eV.[9] Thus, the resolution of our current
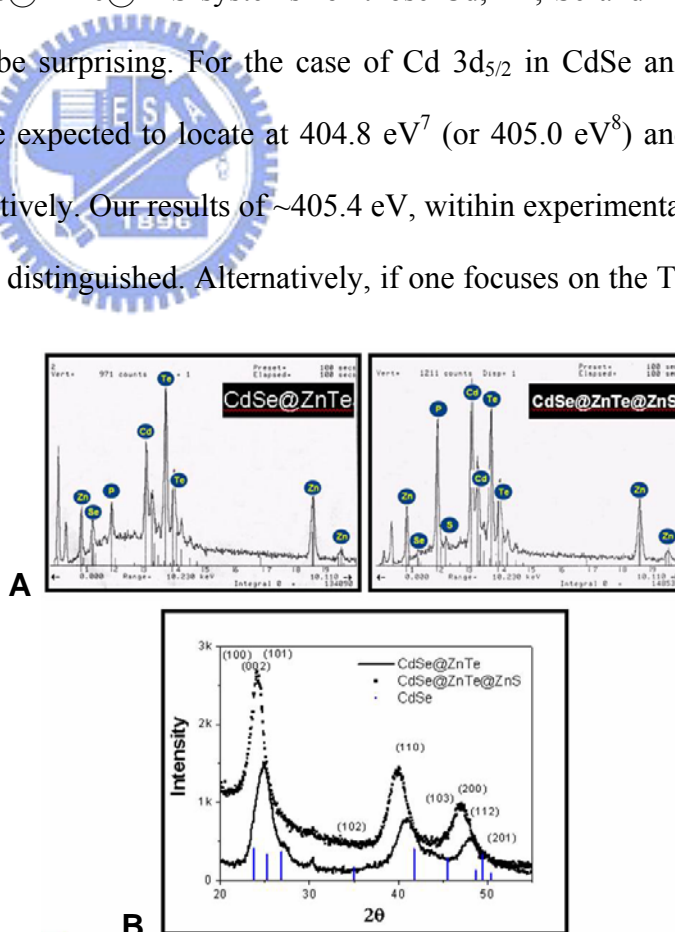
Figure 4.2 A. (upper) Energy dispersive spectroscopy (EDX) characterization of CdSe@ZnTe core/shell (left) and CdSe@ZnTe@ZnS core/shell/shell (right) QDs. B. (lower) X-ray diffraction (XRD) data of CdSe@ZnTe coreshell and CdSe@ZnTe@ZnS core/shell/shell QDs.

120

system is not sufficiently high enough to resolve the origin of the 572.8 eV peak. Simliarly, Zn $2p_{3/2}$ signal in ZnTe predicted to be at 1021.4 eV[9] is also indistinguishable from that of ZnS (1021.4 eV[9]), so that our result of ~1021.4 eV cannot be unqmbiguously assigned to either one. Nevertheless there appears no signal at 1022.0 eV[8] for ZnSe, the results of which, in part, support the lack of alloy formation between CdSe and ZnTe layers in the CdSe@ZnTe@ZnS system. In another angle of XPS approach, the peak intensity ratio for elements of the core and the shell as a function of the electron takeoff angle may serve as a tool for extracting geometrical information about nanoparticles.[10] For example, Piyakis et al.[11] have reported the XPS analysis of spherical Cu nanoclusters by using angle-resolved XPS in combination with Monte Carlo simulation.[11] We have thus made extensive efforts in the angle-tuning studies. Unfortunately, negligible electron-takeoff-angle dependence was observed for the ratio of peak intensities. This result can be tentatively rationalized by the rather thin layer for both ZnTe (0.5 nm) and ZnS (0.4 nm) shell in comparison to CdSe core (3.9 nm in diameter), so that the peak

intensities for Zn and Te (or S) in two shell layers are not sensitive enough to the angle tuning.

Alterntaively, in the following section we will focus on the absorption and luminescence spectroscopy to substantially support our viewpoint of CdSe@ZnTe@ZnS formation. The absorption and
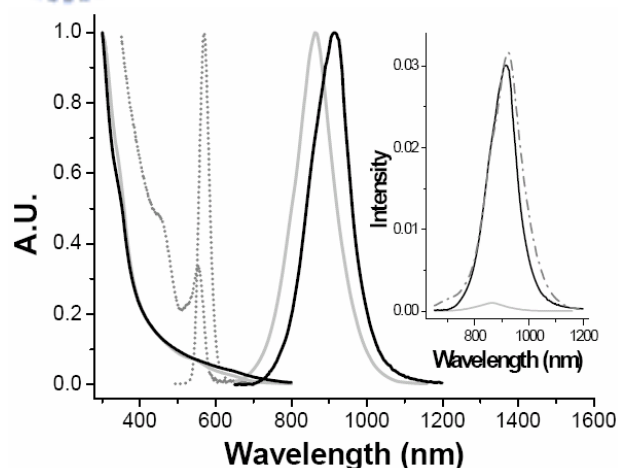
Figure 4.3 The normalized absorption and emission spectra of CdSe core (3.9 nm, dot line), CdSe@ZnTe core/shell (5.0 nm, light grey) and CdSe@ZnTe@ZnS core/shell/shell (5.8 nm, black) QDs in toluene. See Table 4.1 for the corresponding diameters. Insert: The emission intensity of CdSe@ZnTe@ZnS QDs (black: 5.8 nm, dashed line: 6.6 nm) versus that of CdSe@ZnTe QDs (5.0 nm light grey) under an identical experimental condition.

emission spectra of three types of QDs are shown in Figure 4.3.

Table 4.1 Room-temperature photophysical properties for CdSe, CdSe@ZnTe and corresponding CdSe@ZnTe@ZnS QDs

	Size (nm)	PL (λ_{max})	τ_f (ns)	QY (Φ_f)
CdSe[a]	3.9	570	35	0.52
CdSe@ZnTe[a]	5.0	865	55	0.004
CdSe@ZnTe@ZnS[a]	5.8	915	1200	0.12
CdSe@ZnTe@ZnS[a]	6.6	920	1210	0.12
CdSe@ZnTe@ZnS[b]	--[c]	930	950	0.10

[a] TOPO capped QDs in toluene, [b] DHLA capped QDs in water (pH ~7.0), [c] not available due to the aggregation, see text.

Apparently, despite the significant differences in absorption and emission spectra from CdSe (λ_{em} ~ 570 nm) to CdSe@ZnTe (λ_{em} ~ 865 nm),[1] slight red shift in both absorption and emission spectra feature was observed from CdSe@ZnTe to CdSe@ZnTe@ZnS (λ_{em} ~ 915 nm). Note that in general an alloy composite would give a blue shift in both emission and absorption edge.[12] Thus, the red shift in both absorption and emission spectra indirectly prove the CdSe@ZnTe@ZnS (core/shell/shell) structure rather than the alloy formation. Furthermore, it seems unlikely that ZnTe and ZnS would form alloy because of their lattice mismatch, in which the Cd-Se (6.05 Å) lattice is about 12% larger than that of Zn-S (5.41 Å).[12] The resulting emission energy gap may be rationalized by the energy diagram depicted in Scheme 4.1, although the corresponding energetics refer to the bulk materials. As depicted in Scheme 4.1, the lowest energy gap should be ascribed to the ZnTe → CdSe interband transition (~0.8 eV), while the interband transition between ZnTe and ZnS is much higher in energy (~ 1.5 eV) and may have negligible influence on the lower lying transitions.
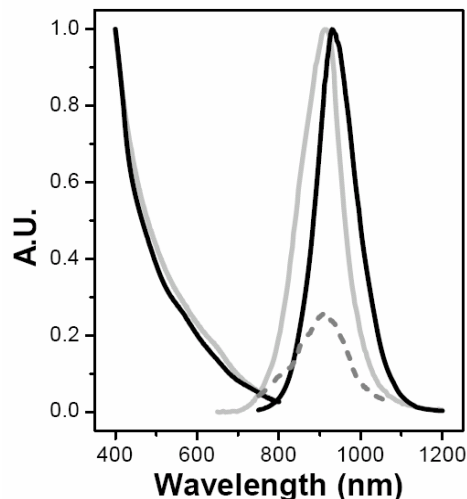
Table 4.1 lists room-temperature emission properties for all three types of QDs with the same core size (and same thickness for ZnTe). While CdSe gave rise to a ligand (TOPO) confined 570-nm emission with quantum efficiency as high as 0.52, the CdSe@ZnTe 865-nm emission is relatively much weaker, with a quantum yield estimated to be 4.0×10^{-3}. Lifetimes (τ_f) for CdSe and CdSe@ZnTe were further measured to be 35 ns and 55 ns, respectively. The radiative decay rate k_r, calculated according to $k_r = \Phi_f/\tau_f$, were then deduced to be 1.5×107 s^{-1} (CdSe) and 7.3×104 s^{-1} (CdSe@ZnTe). Accordingly, the nonradiative decay rates were deduced to be 1.4×107 s^{-1} and 1.8×107 s^{-1} for CdSe and CdSe@ZnTe, respectively. The ~ 200 folds smaller radiative lifetime for the CdSe → ZnTe emission is attributed to the spatially separated electron-hole recombination. As a result, despite the same magnitude of radiationless decay rates in CdSe@ZnTe QDs, its quantum efficiency is much lower than that of CdSe. Drastic increase of the CdSe → ZnTe interband emission intensity was observed after encapulateing ZnS. The quantum efficiency was increased to 0.12, which is ~30 times as large as that of the CdSe@ZnTe. More importantly, the peak wavelength, i.e. the associated CdSe → ZnTe energy gap, changed only slightly, with a slight bathochromic shift from 865 nm to 915 nm, and hence an energy shift of ~1.8 kcal/mol. The small variation of the peak wavelength also supports the aforementioned viewpoint that coating ZnS only affected slightly the CdSe → ZnTe transition due to the well above and below energy levels in the conduction and valence bands, respectively, for ZnS. The increase of quantum efficiency also correlates well with the increase of the observed lifetime to as large as ~1.2 μs. Accordingly, the radiative decay rate was calculated to be 1.0×105 s^{-1}, which, within experimental error, is similar to that of CdSe@ZnTe, indicating negligible interference from ZnS, rather, ZnS plays a key to introduce a barrier to confine holes in ZnTe (see Scheme 4.1). This viewpoint can be further supported by the deduced

radiationless decay rate of 7.3×10^5 s^{-1}. The rather small radiationless decay rate constant in CdSe@ZnTe@ZnS QDs is plausibly due to the hole trapping in ZnTe so that less floats on the outer surface. We further made another synthetic attempt to increase the thickness of ZnS from ~0.4 nm to ~0.8 nm. The increase of average size from ~5.8 to 6.6 nm can be seen from Figure 4.1 (lower-right-side).

Fig. 4.4 The absorption and emission spectra of **a.** (light grey) TOPO capped CdSe@ZnTe@ZnS QDs in toluene, **b**. (black) DHLA capped CdSe@ZnTe@ZnS QDs in water (pH ~ 7) synthesized from batch **a**, **c.** (short dash) the emission of DHLA capped CdSe@ZnTe@ZnS QDs in water excited by 1200 nm laser pulse.
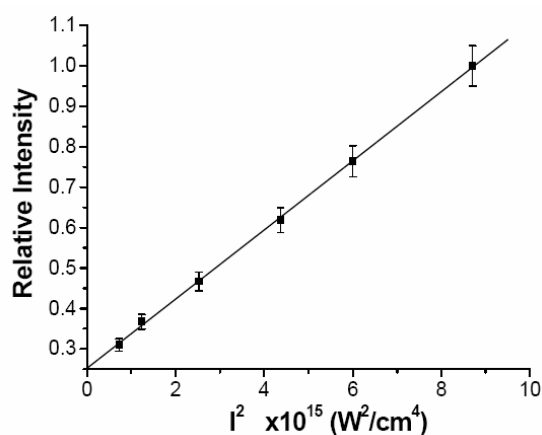
As depicted in the insert of Figure 4.4, the emission peak wavelength only slightly shifted from 915 nm (0.4 nm ZnS) to 920 nm (0.8 nm ZnS), with <3 % increase of quantum efficiency (see **Table 4.1**). Further increase of ZnS thickness to ~1.1 nm show negligible changes on both peak wavelength and emission intensity (not shown here), indicating that ZnS with a thickness of ≥ 0.4 nm should have a good passivation on ZnTe. Figure 4.4 shows the 930-nm emission ($\Phi_f \sim 0.10$) of water soluble, i.e. DHLA capped, CdSe@ZnTe@ZnS QDs. In comparison to its precursor, i.e. TOPO capped CdSe@ZnTe@ZnS QDs ($\lambda_{max} \sim 915$ nm in toluene), the ~15 nm bathochromic shifts of the emission peak are possibly due to the perturbation of different solvent polarities.

Nevertheless, one cannot

Figure 4.5 The plot of 930-nm peak intensity (**I**) for DHLA capped CdSe@ZnTe@ZnS as a function of square of excitation power (λex ~ 1200 nm).

eliminate subtle changes of size distributions during chemical modification. Unfortunately, TEM revealed aggregation of DHLA capped CdSe@ZnTe@ZnS QDs, which prevented further differentiation between TOPO and DHLA capped QDs in size distribution. Measurements of the twophoton absorption cross section were carried out by femtosecond pulse excitation (λ_{ex} ~ 1200 nm, 130 fs). The spectral feature of the emission upon 1200 nm exitation was qualitativley the same as that of one photon excitation (see Figure 4.5). As shown in Figure 4.5, the plot of 930-nm peak intensity versus square of excitation power showed sufficiently linear behavior, supporting the origin of emission from a two-photon absorption process. Taking the absorption extinction coefficient for CdSe (3.9 nm) to be 2.2×10^5 $M^{-1}cm^{-1}$,[13] the DHLA capped CdSe@ZnTe@ZnS concentration was calculated to be 5.8×10^{-7} M in this study. Upon preparing the same concentrsation for both DHLA capped CdSe@ZnTe@ZnS QDs and H_2TPP, the two-photon excited emission intensity for DHLA capped CdSe@ZnTe@ZnS QDs was calculated to be ~20 folds higher than that of H_2TPP. Knowing σ to be 3.5 GM for H_2TPP,[6] σ for CdSe@ZnTe@ZnS QDs was estimated to be ~70 GM.

4.3.2 CdSe@CdTe@ZnTe QDs

Figure 4.6 depicts TEM images and size histograms of CdSe@CdTe (core/shell) and CdSe@CdTe@ZnTe (core/shell/shell) in which the core/shell (CdSe@CdTe) QDs are from the same batch. The size histograms of CdSe@CdTe and CdSe@CdTe@ZnTe QDs were established via counting each individual image over 500 particles. Since the CdSe@CdTe@ZnTe QDs were prepared from the same batch of CdSe@CdTe, it is reasonable to assume the same core/shell size. As an indirect approach, the thickness of ZnTe can be estimated by the subtraction of CdSe@CdTe size from that of the CdSe@CdTe@ZnTe prepared. For QDs shown in Figure 4.6A,

the diameter of CdSe@CdTe and CdSe@CdTe@ZnTe was measured to be in an average of 7.0 and 9.6 nm, respectively. Accordingly, the thickness of ZnTe was estimated to be 1.3 nm. Note that the initial CdSe was prepared to be 3.4 nm (see
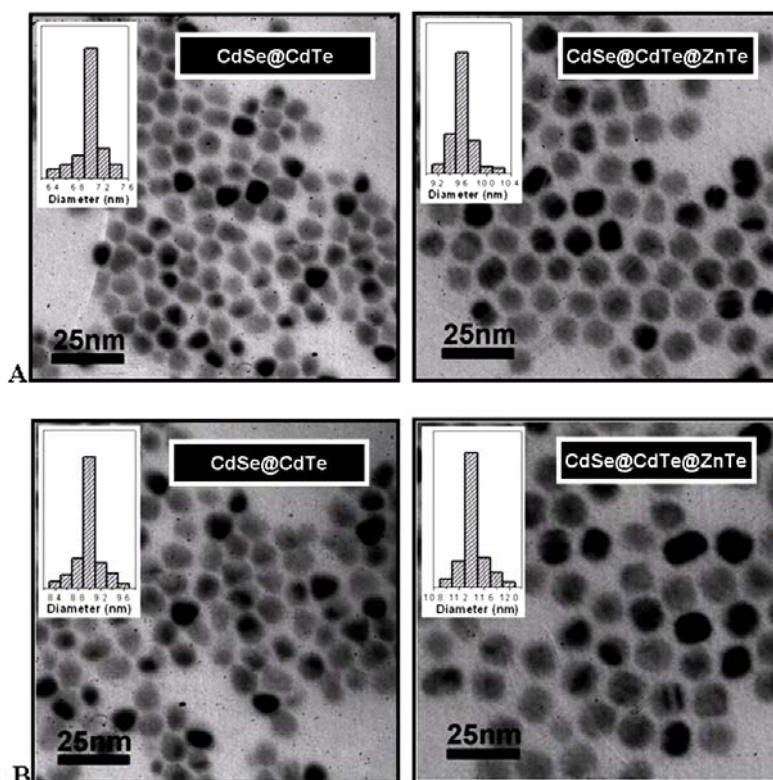

Figure 4.6 TEM images of the samples with an average of (upper-left) 7.0 nm CdSe@CdTe QDs, (upper-right) 9.6 nm CdSe@CdTe@ZnTe QDs; (lower-left) 9.0 nm CdSe@CdTe QDs and (lower-right) 11.4 nm CdSe@CdTe@ZnTe QDs. See Table 4.2 for detailed sizes of core and shell. Insert: Size histograms. The histograms were made via counting over 500 particles in each sample.

Table 4.2) in this batch. In another approach, altering the CdSe core to 5.7 nm was also performed. Accordingly, as shown in Figure 1B, sizes of CdSe@CdTe and CdSe@CdTe@ZnTe were prepared to be 9.0 nm and 11.4 nm, respectively.

The corresponding composition of CdSe@CdTe@ZnTe was characterized by energy dispersive spectroscopy (EDX). As shown in Figure 4.7A, the appearance of Zn peaks at 1.0 and 8.7 KeV, in combination with the decrease of the ratio for Cd versus Te from CdSe@CdTe to CdSe@CdTe@ZnTe, may indirectly support the formation of a ZnTe shell, although the possibility of alloy formation cannot be ruled

out. Furthermore, as shown in Figure 4.7B, comparing the XRD pattern of the CdSe@CdTe core/shell, two sets of peaks at faces (100), (002), (101) and (110), (103), (112) in CdSe@CdTe@ZnTe QDs revealed the same spectral features, with slightly shift to high scattering angle for (110), (103), (112) peaks. Owing to a similar XRD pattern for these two sets of peaks, the formation of an alloy upon encapsulating ZnTe is not likely. Nevertheless, similar to the results of EDX, the X-ray data could not definitely conclude a core/shell/shell structure.
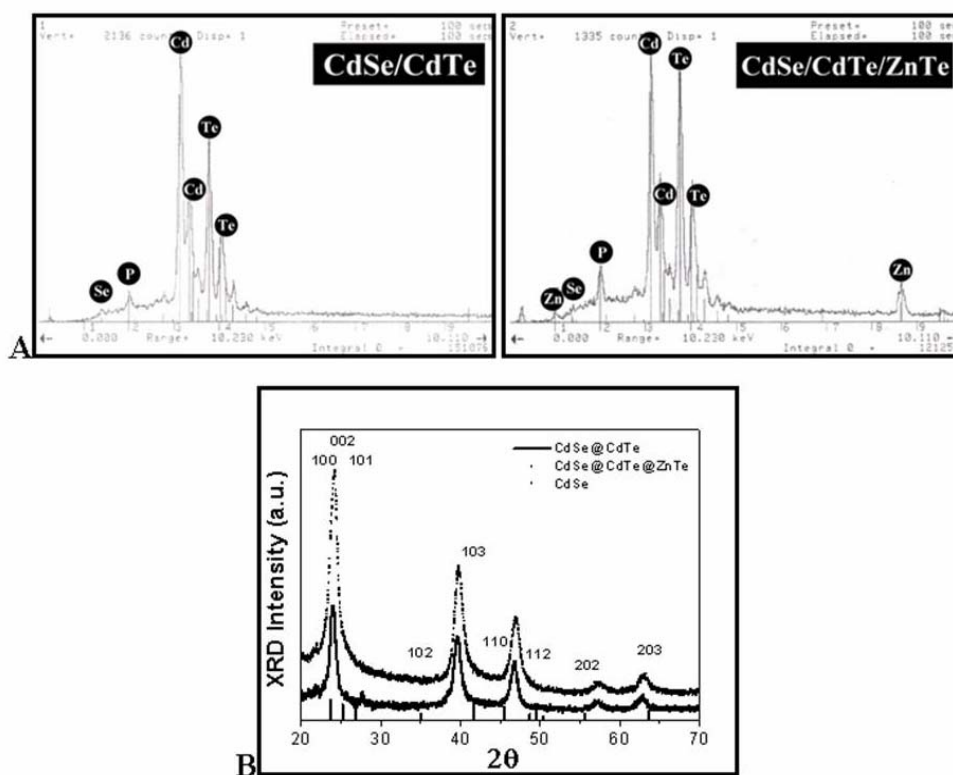

Figure 4.7 **A.**(upper) Energy dispersive spectroscopy (EDX) characterization of CdSe@CdTe core/shell (left) and CdSe@CdTe@ZnTe core/shell/shell (right) QDs. B. (lower) X-ray diffraction (XRD) data of CdSe@CdTe core/shell and CdSe@CdTe@ZnTe core/shell/shell QDs.

In theory, XPS analyses may provede more composition information we have further made efforts to perform XPS analyses. However, due to the same Te element in both CdTe (shell) and ZnTe (shell) structures, the characteric bands associated with either shell/sehll or alloy composition are theoretically undistinguishable. This makes XPS analyses to differentiate core/shell/shell and alloy structures infeasible.

Alternatively, as for another angle of XPS approach, the peak intensity ratio for elements of the core and the shell as a function of the electron takeoff angle may serve as a tool to extract geometrical information about nanoparticles.[10] Piyakis et al.[11] have recently reported the XPS analysis of spherical Cu nanoclusters by using angle-resolved XPS in combination with Monte Carlo simulation.[11] Accordingly, the peak intensity ratio for elements of core versus shell as a function of the electron takeoff angle may serve as a valuable tool to extract geometrical information about nanoparticles.[7] If QDs were entirely composed of an alloy, the relative peak intensities for Cd, Se, Zn and Te would be independent of the electron takeoff angle. Empirically, the ratio of peak intensity at 90° and 54.7° for X-ray sources is estimated to be 0.867, 0.905, 0.900 and 0.863 for $Cd(3d_{5/2})$, $Se(3d)$, $Zn(2p_{3/2})$ and $Te(3d_{5/2})$, respectively.[8] It means, upon normalizing the Zn peak intensity, the peak intensity ratio for Cd (90°) / Cd (54.7°) is deduced to be 0.96 for the case of a single alloy. Accordingly, deviation from this value is expected for a multilayer such as the core/shell structure. In the case of CdTe@CdSe (see Chapter 3), we have successfully proved the core/shell structure with larger divergence of Se/Te ratio. However, in this case of CdSe@CdTe@ZnTe, larger divergence can only prove the QDs are not an entire alloy, even if the extra-thin layers could still be observed the variations. No matter if the fusion occured between the shells or between the core and the first layer, it would also show deviation. In fact, because of the rather thin layer for both CdTe and ZnTe shell in comparison to CdSe core, the peak intensity for Cd is mainly attributed to that of core and hence is not sensitive enough to the angle tuning. More evidence of the CdSe@CdTe@ZnTe core/shell/shell structure is provided in the following section of photophysical studies.

The absorption and emission spectra of three types of QDs are shown in Figure 4.8, and the corresponding spectral and dynamic parameters are listed in Table 4.2. As

shown in Figure 4.8, tuning type-I CdSe (core only) to the type-II CdSe@CdTe QDs significantly alters both absorption and emission spectra (see Figure 4.8), in which the transition switches from the core emission (λ_{em} ~550 nm) in CdSe to the
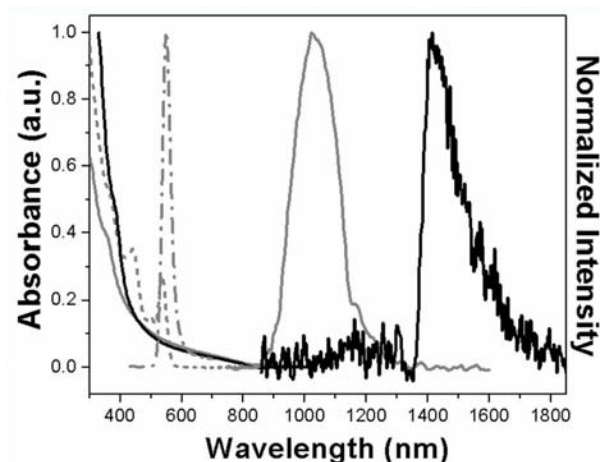
Figure 4.8 The normalized absorption and emission spectra of CdSe core (3.4 nm, short dash), CdSe@CdTe (3.4/1.8 nm) core/shell (grey) and CdSe@CdTe@ZnTe (3.4/1.8/1.3 nm) core/shell/shell (black) QDs in toluene. See Table 4.2 for other photophysical parameters.

CdSe → CdTe interband emission (λ_{em} ~1026 nm) in the CdSe@CdTe structure. Furthermore, the quantum efficiency ($\Phi_f \sim 1.2 \times 10^{-3}$) of the 1026 nm interband emission is significantly lower than that ($\Phi_f \sim 0.28$) of the corresponding 550 nm core-only emission. The results can be rationalized by the separation of electron and hole into CdSe and CdTe, respectively. Accordingly, a long radiative lifetime, i.e. a small radiative rate constant for the electron/hole recombination, is expected. The long-lived hole carrier floating on the surface of CdTe is further subject to either defect trapping or quenching via surrounding stimuli such as colloids, solvent moleucles, etc, resulting in a significant reduction of the interband emission.

As depicted in Figure 4.8, encapsulating CdSe@CdTe by an additional shell ZnTe, forming a CdSe@CdTe@ZnTe structure, did not cause appreciable changes in lower-lying absorption spectra. In sharp contrast, however, the characteric 1026 nm emission in CdSe@CdTe (3.4/1.8 nm) nearly disappeared, accompanied by the apeparance of a very weak, long wavelength emission maximized at 1415 nm. This result may not be surprising since the introduction of ZnTe, forming CdSe@CdTe@ZnTe QDs, creates an additional cascade channel for the hole carrier.

Upon excitation, if both electron and hole undergo ultrafast transport, the lowest lying energy gap should be in between CdSe and ZnTe transtion. On this basis, the 1415 nm emission band fits well to the energy gap of 0.8 eV between CdSe and ZnTe predicted from the bulk materials (see Scheme 4.1), and is tentatively assigned to the CdSe $\rightarrow$ ZnTe transition. However, due to the relatively weak emission intensity, its origin from the deep-trap emission is also possible. We have thus made an attempt to increase the thickness of ZnTe from ~1.3 nm to ~1.8 nm.

Table 4.2. Room-temparature photophysical properties for CdSe, CdSe@CdTe and CdSe@CdTe@ZnTe QDs in toluene.

|	Size (nm)	PL (λ_{max})	Φ_f	τ_f (ns)	Radiative lifetime
CdSe	3.4	550	0.28	20	72 ns
	5.7	648	0.31	23	74 ns
CdSe@CdTe	7.0[a]	1026	1.2×10^{-3}	30	25 μs
	9.0[c]	1090	1.0×10^{-3}	27	27 μs
CdSe@CdTe@ZnTe	9.6[a]	1415	1.5×10^{-5}	150	10 ms
	10.6[b]	1470	1.3×10^{-5}	115	8.8 ms
	11.4[c]	1518	1.1×10^{-5}	120	11 ms

[a] CdSe = 3.4 nm, ZnTe = 1.3 nm (thickness), [b] CdSe = 3.4 nm, ZnTe = 1.8 nm (thickness), [c] CdSe = 5.7 nm, ZnTe = 1.2 nm

As shown in Table 4.2, the corresponding emission peak wavelength shifts from 1415 nm (1.3 nm ZnTe) to 1470 nm (1.8 nm ZnTe). In another approach, we altered the CdSe core size from 3.4 nm to 5.7 nm, while the shell thickness for both CdTe and ZnTe, within experimental uncertainty, remained unchanged. As a result, the emission red shifted from 1415 nm to 1518 nm. The results correlate well with the increase (decrease) of the ZnTe valence (CdSe conduction) band edge, resulting in a decrease of the CdSe $\rightarrow$ ZnTe transition. Due to the systematic variation of the peak

wavelength as a function of the ZnTe thickness, the possibility that the 1415 nm band originating from the deep-trap emission can be ruled out. It is also noteworthy that in general an alloy composite would give a blue shift in both emission and absorption edge.[12] Thus, the red shift in both absorption and emission spectra of the CdTe → ZnTe transition shown in Figure 4.8 and Table 4.2 indirectly prove the CdSe@CdTe@ZnTe (core/shell/shell) structure rather than the alloy formation.

Table 4.2 lists room-temperature emission properties for all three types of QDs with the same core size (and the same shell thickness for CdTe). While CdSe (3.4 nm) gave rise to a ligand (TOPO) confined 550-nm emission with quantum efficiency as high as 0.28, the 1026-nm emission in CdSe@CdTe QDs (3.4/1.8 nm) is relatively much weaker, with a quantum yield estimated to be 1.2×10^{-3}. Lifetimes (τ_f) for CdSe (3.4 nm) and CdSe@CdTe (3.4/1.8 nm) were further measured to be 20 ns and 30 ns, respectively. The radiative decay rate k_r, calculated according to $k_r = \Phi_f/\tau_f$, were then deduced to be 1.4×10^7 s^{-1} (CdSe) and 4.0×10^4 s^{-1} (CdSe@CdTe).

Accordingly, the nonradiative decay rates were deduced to be 3.6×10^7 s^{-1} and 3.3×10^7 s^{-1} for CdSe and CdSe@CdTe, respectively. The > 300 folds smaller radiative lifetime for the CdSe → ZnTe emission is attributed to the spatially separated electron-hole recombination (vide supra). As a result,
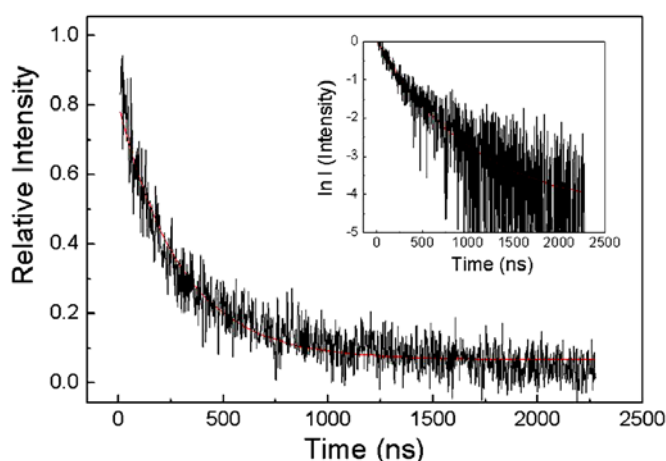
Figure 4.9   The decay profile of CdSe@CdTe@ZnTe (3.4/1.8/1.3 nm) core/shell/shell QDs in toluene monitored at 1400 ± 20 nm (λ_{ex} = 532 nm). In this decay profile a < 6 ns decay component resulting from the scattering of fundamental laser light (1064 nm) has been removed. Insert: The logarithm of emission intensity and its first-order linear fit (red line). Note that the decay was fitted by Ae^{-kt} + B where B is an offset value, k was fitted to be 6.7×10^3 s^{-1} (τ_f ~150 ns).

despite the same magnitude of radiationless decay rates in CdSe@CdTe QDs, its quantum efficiency is much lower than that of CdSe. For the case of CdSe@CdTe@ZnTe QDs, the radiative lietime of CdSe $\rightarrow$ ZnTe transition, being separated by CdTe, is expectd to be enormously long; consequently the relaxation dynamics may be dominated by the radiationless transition. This viewpoint is supported by the quantum yield of ~1.5 $\times 10^{-5}$ for the 1415 nm emission band. As depicted in Figure 4.9, the decay trace of the 1415 nm emission band revealed a single exponential kinetics and a liftetime of 150 ns was then extracted. Accordingly, the radiative lifetime of CdSe $\rightarrow$ ZnTe emission was deduced to be as long as ~10 ms. Similar radiative decay times in the range of milliseconds were deduced for CdSe@CdTe@ZnTe QDs upon varying either core (CdSe) or shell (ZnTe) sizes (see Table 4.2).

One interesting featue is in that the 1026 nm (CdSe $\rightarrow$ CdTe) emission observed in CdSe@CdTe (3.4/1.8 nm) disappeared in the the CdSe@CdTe@ZnTe structure. Upon carefully examining the emission spectra associated with CdSe@CdTe@ZnTe, trace emission in the region of 1100−1250 nm with λ_{max} ~ 1150 nm may not be neglected. Taking account of the subtle interfacial interaction and lattice mismatch that may cause slight changes of the band edges, it is reasonable to assign this weak band to the CdSe $\rightarrow$ CdTe interband emission (1026 nm) obsereved in CdSe@CdTe QDs. However, in view of the band gaps associated with CdSe@CdTe@ZnTe structure (Figure 4.6), one cannot eliminate the possibility that the emission originats from CdTe $\rightarrow$ ZnTe transition (1.2 eV in bulk) or from a mixing of CdSe $\rightarrow$ CdTe and CdTe $\rightarrow$ ZnTe due to the accidental degeneracy between these two transition gaps (1.2 eV in bulk, see Scheme 4.1). We have made efforts in an attempt to resolve the relaxation dynamics of the extremely weak 1150 nm emission. However, the decay rate is too fast to be resolved by our NIR system with a response time of ~50 ps. It is

reasonable to assume a similar radiative lifetime for the CdSe $\rightarrow$ CdTe emission between CdSe@CdTe and CdSe@CdTe@ZnTe QDs. Taking 25 μs and < 10^{-6} for the radiative lifetime and quantum yield, respectively, for the 1150 nm (CdSe $\rightarrow$ CdTe) emission, one then deduces an observed lifetime of < 25 ps, consistent with the irresolvable relaxation dynamics experimentally. If the decay of CdSe $\rightarrow$ CdTe emission is dominated by the electron/hole separation, the results support ultrafast electron (or hole) transfer in this CdSe@CdTe@ZnTe structure with cascade band edges. In other words, independent of excitation at CdSe, CdTe or ZnTe layers, rates of electron and hole separation are ultrafast, resulting in a unique, lowest lying CdSe $\rightarrow$ ZnTe emission. Focus on the femtosecond transient absorption in order to resolve the early relaxation dynamics is currently in progress.

4.4. Conclusions

In conclusion, syntheses of CdSe@ZnTe@ZnS and CdSe@CdTe@ZnTe (core/shell/shell) type-II QDs from CdSe@ZnTe and CdSe@CdTe, respectively, have been achieved. To beginning with, in comparison to that of type-II CdSe@ZnTe, although the addition of ZnS only changed the interband emission peak wavelength slightly, CdSe@ZnTe@ZnS QDs give rise to ~30 folds enhancement of the quantum efficiency (Φ_f ~0.12). By encapsulating DHLA, water soluble CdSe@ZnTe@ZnS (3.9 nm/0.5 nm/0.4 nm) was prepared, and it exhibited an interband emission at ~930 nm with a fluorescence yield of ~0.1. Femtosecond pulse (λ_{ex} ~ 1200 nm) excitation measurement derives a two-photon absorption cross section, σ, of ~70 GM, supporting its suitability for the use as near infrared dyes for biomedical imaging by taking advantage of their great photostability and deeper light penetration. On the second division, in order to compare with the strong CdSe (core only, 3.4 nm)

emission (λ_{max} ~550 nm, Φ_f ~0.28), moderate CdSe → CdTe emission (λ_{max} ~1026 nm, Φ_f ~1.2 × 10^{-3}) for CdSe@CdTe (core/shell, 3.4 nm/1.8 nm), rather weak CdSe → ZnTe interband emission (λ_{max} ~1415 nm, Φ_f ~1.5 × 10^{-5}) was resolved for the CdSe@CdTe@ZnTe structure (3.4/1.8/1.3 nm). Capping ZnTe to CdSe@CdTe results in a far electron-hole separation between CdSe and ZnTe via an intermediate layer CdTe. In the case of CdSe@CdTe@ZnTe structure (3.4/1.8/1.3 nm), a lifetime of as long as 150 ns was observed for the CdSe → ZnTe 1415 nm emission. The result further deduces an enormously long radiative lifetime of ~10 ms due to the spatial separation of electron and hole via the CdTe intermediate layer. In the case of CdSe@CdTe@ZnTe structure, upon excitation, the float of long-lived charge separation may serve as an excellent hole-carrier for catalyzing the oxidation reaction. Attempts have also been made in synthesizing the ZnTe@CdTe@CdSe type-II QDs, in which the order of band edges is reversed with respect to the CdSe@CdTe@ZnTe structure, so that the electron can be floated in the CdSe layer to carry out the reduction reaction. However, at this stage, this pathway failed due to the difficulty in synthesizing ZnTe core QDs. Focus on circumeventing this obstacle is currently in progress.

4.5 References

1   Chen, C. Y.; Cheng, C. T.; Yu, J. K.; Pu, S. C.; Cheng, Y. M.; Chou, P. T.; Chou, Y. H.; Chiu, H. T., *J. Phys. Chem. B*, **2004**, *108*, 10687.

2   Mattoussi, H.; Mauro, J. M.; Goldman, E. R.; Anderson, G. P.; Sundar, V. C.; Milkulec, F. V.; Bawendi, M. G., *J. Am. Chem. Soc.*, **2000**, *122*, 12142.

3   Gunsalus, I. C.; Barton, L. S.; Gruber, W., *J. Am. Chem. Soc.*, **1956**, *78*, 1763.

4   Peng, Z. A.; Peng, X., *J. Am. Chem. Soc.* **2002**, *123*, 183.

5   Benson, R. C.; Jues, H. A., *J. Chem. Eng. Data.* **1977**, *22*, 379.

6   Karotki, A.; Drobizhev, M.; Kruk, M.; Spangler, C.; Nickel,E.; Mamardashvili, N., *J. Opt. Soc. Am. B* **2003**, *20*, 321.

7   Briggs, D.; Seah, M. P., John WILLEY & SONS. *Vol. 1*, second edition, **1993**.

8   Wagner, C. D.; Moulder, J. F.; Davis, L. E.; Riggs, W. M., Perking-Elmer Corporation, Physical Electronics Division (end of book).

9   Ebert, H.; Knecht, M.; Muhler, M.; Helmer, O.; Bensch, W., *J. Phys. Chem.* **1995**, *99*, 3326.

10 Tunc, I.; Suzer, S.; Correa-Duarte, M. A.; Liz-Marzan, L. M., *J. Phys. Chem. B* **2005**, *109*, 7597.

11 Piyakis, K. N.; Yang, D. Q.; Sacher, E., *Surf. Sci.* **2003**, *536*, 139.

12 Malik, M. A.; O'Brien, P., N. Revaprasadu, *Chem. Mater.* **2002**, *14*, 2004.

13 Yu, W. W.; Qu, L.; Guo, W.; Peng, X., *Chem. Mater.* **2003**, *15*, 2854.

Chapter 5   Concluding Remarks

In conclusion, as summarized in Scheme 5.1, we have demonstrated that the different designs/fabrications of the core/shell (core/shell/shell) structures produced the different optical and physical properties and can well be used of various applications.

Seeing that the outstanding propertices among the optical and electrical fields of type-I and Type-II core/shell QDs discussed before, there are lots of researchable directions and applications could be going to. Furthermore, it also figures out the brightening prospects for core/shell (core/shell/shell) QDs investigation. Herein, we comment some achievements in the following.
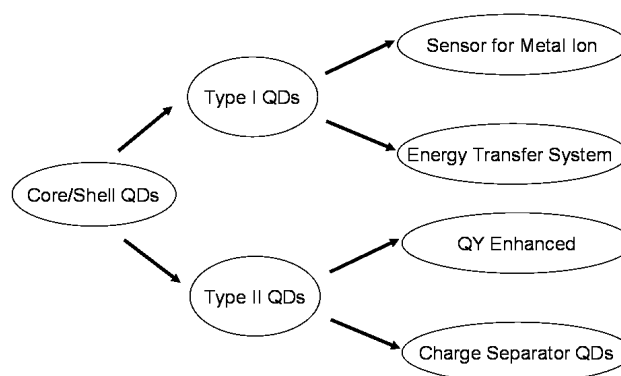

Scheme 5.1 Summary of Explorations

5.1. Studies Related to Type-I CdSe@ZnX (X=S, Se) Core/Shell QDs

Although various applications of Type-I core/shell QDs have been reported and introduced at section 1.2.1, two novel applications were achieved in Chapter 2. There, the strategy of one-pot syntheses of CdSe@ZnX QDs and its associated wavelength tunability and suitability were elaborated. So far as convenience is concerned, it is undoubted that one-pot reaction scheme can shorten the reaction time, whereas the fine-tuning of color is still feasible.

Besides, we have demonstrated a practical system based on DHLA capped CdSe@ZnS (core/shell) QDs to fluorogenically probe Hg^{2+} in aqueous solution and solid film at room temperature. Submicromolar sensitivity has been achieved and this sensor is found to be highly selective, being insensitive to other metal ions of concern as drinking water pollutants. The high quantum yield, narrow-bandwidth and impurity-emission-free fluorescence make this DHLA capped CdSe@ZnS QDs suitable to monitor Hg^{2+} environmentally.

Moreover, energy transfer system was designed. CdSe@ZnS QDs modified with 15-crown-5 in water were exhibitd with excellent selectivity toward K^+. Single transduction has been achieved by precipitation and resulted in the quenching of the fluorescence. In a qualitative manner, other than extending the sensitivity range, we present the dual color energy transfer method as a general detection scheme, which renders a great versatility and flexibility in view of future applications.
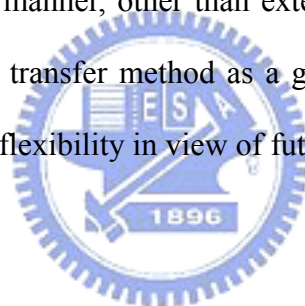
5.2. Studies Related to Type-II CdSe@ZnTe and CdTe@CdSe Core/Shell QDs

Based on a colloidal template, even an exquisite synthetic route to type-II CdSe@ZnTe and CdTe@CdSe (core/shell) QDs was achieved. The corresponding data on CdSe@ZnTe is obscure. Contrast to the thorough investigations of the electron/hole relaxation pathways on the type-I nanoparticles discussed, to our knowledge, dynamics of the interfacial electron/hole separation for these type-II QDs has not been systematically studied. We present the spectroscopy and femtosecond upconversion approaches in Chapter 3 for type-II QDs, CdSe@ZnTe and CdTe@CdSe. The results indicate that the rate of electrons and holes transfer decrease

with the increasing in the size of the cores, and is independent of shell-thickness in the type-II core/shell QDs. We believe that especially the degree of control on the rate of electron transfer, can be crucial in applications where rapid carrier separation followed by charge transfer into a matrix or electrode is important, as in photovoltaic devices. Within this view point, the major relaxation process of type-II core/shell QDs was not the emission of electromagnetic waves. Instead, electrons and holes are mainly ejected into the surroundings. Based on their unique properties, we anticipate that the type II QDs might also be used as a catalyst in the redox reaction with its particular electron donner/acceptor capabilities.

5.3. Studies Related to Type-II CdSe@ZnTe@ZnS and CdSe@CdTe@ZnTe Core/Shell/Shell QDs

One intriguing potential of the type II QDs is to greatly extend the lifespan of the charge separation, so that either electron or hole floating on the outmost shell region can be further exploited in variety of applications. In view of this goal we have carried out the following design strategy toward a core/shell/shell type II QDs in Chapter 4. Two types of structures A (CdSe@ZnTe@ZnS) and B (CdSe@CdTe@ZnTe), shown in Scheme 4.1A, have been synthesized. In order to enhance the quantum yield of type-II CdSe@ZnTe QDs (Φ_f ~0.004) a layer of ZnS is applied to the QDs. Although the addition of ZnS only changed the interband emission peak wavelength slightly, CdSe@ZnTe@ZnS QDs give rise to ~30 folds enhancement of the quantum efficiency (Φ_f ~0.12). By encapsulating CdSe@ZnTe@ZnS in DHLA, water soluble QDs were prepared. This material exhibited an interband emission at ~930 nm with a fluorescence yield of ~0.1. The results indicated the possibility to synthesize environmentally safer core/shell materials with extended tunable emission ranges. We

also performed femtosecond pulse excitation of the QDs at $\lambda_{ex} \sim 1200$ nm. The emission for the process supports a two-photon absorption mechanism. By employing this theory and setting up two crossing light sources, we anticipate they will be suitable for the use as NIR dyes for bio-imaging by taking advantage of their great photostability and deeper light penetration.

Last, on the charge separator QDs, shown in Scheme 4.1B, in comparison with the strong CdSe (core only) emission ($\Phi_f \sim 0.28$), moderate CdSe $\rightarrow$ CdTe emission ($\Phi_f \sim 1.2 \times 10^{-3}$) for CdSe@CdTe (core/shell), and rather weak CdSe $\rightarrow$ ZnTe interband emission ($\Phi_f \sim 1.5 \times 10^{-5}$) was resolved for the CdSe@CdTe@ZnTe structure. Capping ZnTe to CdSe@CdTe resulted in the formation of CdTe as an intermediate layer. The consequence is a further separation of the electrons in the CdSe core and the holes in the ZnTe shell. A lifetime of as long as 150 ns was observed for the CdSe $\rightarrow$ ZnTe emission. The result further deduces an enormously long radiative lifetime of ~10 ms due to the spatial separation of electron and hole via the CdTe intermediate layer. Upon excitation, the long-lived charge separation may serve as an excellent hole-reservoir for catalyzing oxidation reactions. Attempts have also been made in synthesizing ZnTe@CdTe@CdSe type-II QDs. For this structure, the order of band edges is reversed with respect to the CdSe@CdTe@ZnTe structure. In principle, the electrons can be floated in the CdSe layer to carry out reduction reactions. However, at this stage, the exploration failed due to the difficulty in synthesizing ZnTe core QDs. Focus on circumventing this obstacle is currently in progress.